NUMERICAL SIMULATIONS OF ELECTROHYDRODYNAMIC EVOLUTION OF THIN POLYMER FILMS

A Thesis
Submitted to the Graduate Faculty
of the
North Dakota State University
of Agriculture and Applied Science

By

Joshua Christopher Borglum

In Partial Fulfilment of the Requirements
For the Degree of
MASTER OF SCIENCE

Major Department:
Mechanical Engineering

August 2015

Fargo, North Dakota

North Dakota State University
Graduate School

Title

Numerical Simulations of Electrohydrodynamic Evolution of Thin Polymer Films

By

Joshua Christopher Borglum

The Supervisory Committee certifies that this ***disquisition*** complies with North Dakota State University's regulations and meets the accepted standards for the degree of

MASTER OF SCIENCE

SUPERVISORY COMMITTEE:

Dr. Xiangfa Wu
Chair

Dr. Yildirim Bora Suzen

Dr. Yechun Wang

Dr. Xuefeng Chu

Approved:

10/29/15
Date

Dr. Alan Kallmeyer
Department Chair

ABSTRACT

Recently developed needleless electrospinning and electrolithography are two successful techniques that have been utilized extensively for low-cost, scalable, and continuous nano-fabrication. Rational understanding of the electrohydrodynamic principles underneath these nano-manufacturing methods is crucial to fabrication of continuous nanofibers and patterned thin films. This research project is to formulate robust, high-efficiency finite-difference Fourier spectral methods to simulate the electrohydrodynamic evolution of thin polymer films. Two thin-film models were considered and refined. The first was based on reduced lubrication theory; the second further took into account the effect of solvent drying and dewetting of the substrate. Fast Fourier Transform (FFT) based spectral method was integrated into the finite-difference algorithms for fast, accurately solving the governing nonlinear partial differential equations. The present methods have been used to examine the dependencies of the evolving surface features of the thin films upon the model parameters. The present study can be used for fast, controllable nanofabrication.

TABLE OF CONTENTS

LIST OF TABLES

LIST OF FIGURES

LIST OF SYMBOLS

H.....Height of the top electrode

H.....Height of the evolving film, measured as the distance from the bottom electrode

J.....Pressure flux

∇ .....Del operator

μ .....Viscosity

$\vec{v}$ .....Velocity

p .....Pressure

t .....Time

ε_0 .....Permittivity of free space

ε .....Relative dielectric constant

E .....Drying rate

E_a .....Electric field in air phase

E_p .....Electric field in polymer phase

ψ .....Electric potential

U.....Voltage

γ .....Surface tension

A.....Hamaker constant

h_m .....Depth of mask, measured as the distance from the top electrode.

L .....Length

ρ .....Radius of curvature

k.....Wave number

h_* .....Height of bottom substrate

C.....Distribution density of defect pattern

θ_e .....Contact angle (^{o})

λ .....Wavelength

ω .....Wave dispersion relation

c.....Polymer volume Fraction

a.....Viscosity exponent

v.....Evaporation exponent

D.....Diffusion constant

1. INTRODUCTION

With the development of electrospinning technology in the past two decades, a variety of electrospun nanofibers of polymers and polymer-derived carbon, metals, ceramics, and semiconductors have been successfully produced for use in broad fields. Electrospun nanofibers carry many unique properties, such as their continuity, high surface-to-volume ratio, ability to form ultrathin, strong, porous membranes, and feasible tailorability in fiber diameter, morphology and chemical structure. These unique properties have provided rapidly increasing opportunities in broader fields such as materials science, biomedical engineering, and energy production. So far, electrospun fibers have been used in tissue engineering scaffolds, air/liquid filtration, sensors, and energy conversion and storage (e.g., electrodes of lithium-ion rechargeable batteries and supercapacitors).

Similar to other conventional and concurrent nanofabrication techniques, the control parameters of electrospinning process influence the properties of electrospun fibers. It has been found that nanofibers with different morphologies can be fabricated by varying the material used, solution properties, spinneret design, and environment (Li & Xia, 2004). Today many electrospun fibers with unique morphologies have been produced such as the grooved fibers, porous fibers, ribbon fibers, helical fibers, hollow fibers, core/sheath, crimped, and beaded fibers. It is essential to formulate rational models to simulate the electrospinning process for predicting the fiber morphology and properties for various materials, solutions, and applications. Therefore, efficient, high-accuracy models capable of predicting the fiber formation in electrospinning based on the basic material properties (e.g., solution concentration, viscosity, and dielectric constant, etc.) and process parameters (e.g., spinneret structure, electric voltage, span between the spinneret and the collector, etc.) are still highly desired.

Substantial experimental investigations on the fabrication and properties of electrospun fibers have been performed and reported in the literature in the past two decades. In contrast, only a few theoretical models have been made in the literature regarding the jet initiation, stretching, and whipping stability (Reneker, et al., 2007). In principle, an accurate, rational model for the electrospinning process should take into account the entire formation of the fiber, which includes the jet initiation from the solution, jet stretching, whipping instability, and drying. So far, no modeling work has been available yet in the literature to take into account the entire electrohydrodynamic process of electrospinning.

On the other hand, electrohydrodynamic self-assembly (electrolithography) of polymer melts has been studied extensively in both experimental and theoretical investigations, which provides insight into the phenomenon of recently developed needleless electrospinning process for continuous, scalable nanofiber fabrication. Lithographically induced self-assembly is a process by which ultrathin polymer melts can form into periodic patterns due to electrohydrodynamic destabilization (Chou & Zhuang, 1999). Quite a few studies have been conducted on the simulation and prediction of the self-assembled patterns formed at the surface of thin films of polymer melts. These models, accurate for the lithographically induced self-assembly (LISA) process, would not be capable of fully capturing the electrohydrodynamics of electrospun solutions due to the mono-phase properties of the polymer melts. To gain an efficient, accurate model for the electrospinning process, the existing electrohydrodynamic models used to predict the self-assembly process of polymer melts need to be altered to allow for two phase solutions and melts with varying properties.

The purpose of this thesis work was to extend the existing theoretical work in the self-assembly process for modelling the initiation of jets from a polymer solution in needleless

electrospinning process. The research project was to formulate robust, high-efficiency finite-difference Fourier spectral methods to simulate the electrohydrodynamic evolution of thin polymer films, particularly the surface destabilization under electrostatic field. Two electrohydrodynamic thin-film models were considered and refined. The first was based on reduced lubrication theory; the second further took into account the effect of solvent evaporation and dewetting of the substrate. Fast Fourier Transform (FFT) based spectral method was integrated into the finite difference algorithms for fast, accurately solving the resulting governing nonlinear partial differential equations (PDEs). The present methods have been used to examine the dependencies of the evolving surface features of the thin films upon the model parameters, e.g., the dielectric constants, film thickness, mask shape and thickness, etc. Numerical results obtained by the present simulations were validated by those available in the literature. The present study can be used for fast, controllable nanofiber fabrication based on needleless electrospinning technique.

2. LITERATURE REVIEW

2.1. Nanofiber Electrospinning

Electrospinning is a low-cost, top-down nanofabrication technique, which is based on electrohydrodynamics for producing ultra-thin continuous fibers with the diameters in the range from 1 nm to micrometers (Reneker & Chun, 1996; Dzenis, 2004; Reneker et al., 2007).

Figure 2.1 shows a basic needle-based electrospinning setup, which consists of a power supply, a nozzle, a syringe, and a counter electrode.

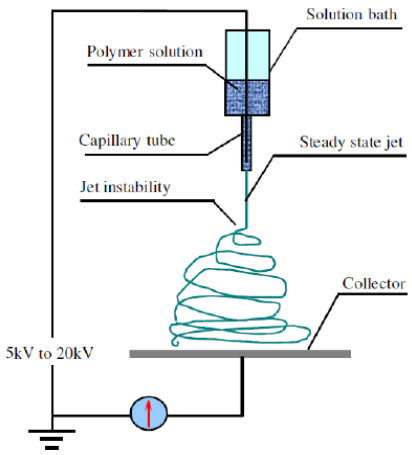

Figure 2.1: A typical apparatus for needle electrospinning.

Based on such an electrospinning setup, polymer solutions are typically used as the spinning liquids. When a DC voltage is gradually increased between the two electrodes (i.e., the needle and the fiber collector), a droplet first forms at the tip of the needle, which experiences a strong electrostatic force induced by the electrostatic field between the counter electrode collector and the needle. These electrostatic forces deform the droplet into a cone shape called a "Taylor cone" (Taylor 1969; Yarin et al. 2001). Once the electrostatic forces break the surface tension of the "Taylor cone", a jet is formed from the tip of the "Taylor cone". Figure 2.2 shows the experimental observation of a "Taylor cone" and a straight jet.

Figure 2.2: Taylor cone and jet initiation from a capillary needle.

The interaction with the electric field and repulsion of charges inside the jet causes the jet to stretch. As the jet stretches, it begins to whip. The whipping phenomenon is a kind of electrohydrodynamic destabilization which assists the significant thinning and drying of the polymer jet. Evaporation of the solvent from the jet allows the jet to solidify into fibers. The above experimental setup of electrospinning has been used in laboratories around the world for research on electrospinning and electrospun nanofibers.

Electrospun nanofibers are usually fabricated from polymeric solutions. In reality, electrospinning has also been used to produce ultrathin fibers from ceramics, metals, carbon, semiconductors and many other variations of materials. The diameter of electrospun fiber diameter ranges from several nanometers to a few microns (Greiner & Wendorff, 2007). A round cross-sectional fiber is the most widely fabricated. In practice, nanofibers of many different morphologies can be fabricated by controlling the polymer/solvent properties, nozzle geometries, and environmental conditions (Bognitzki et al., 2001; Li & Xia, 2004). Figure 2.3 shows the images of beaded, round, hollow, and porous electrospun fibers.

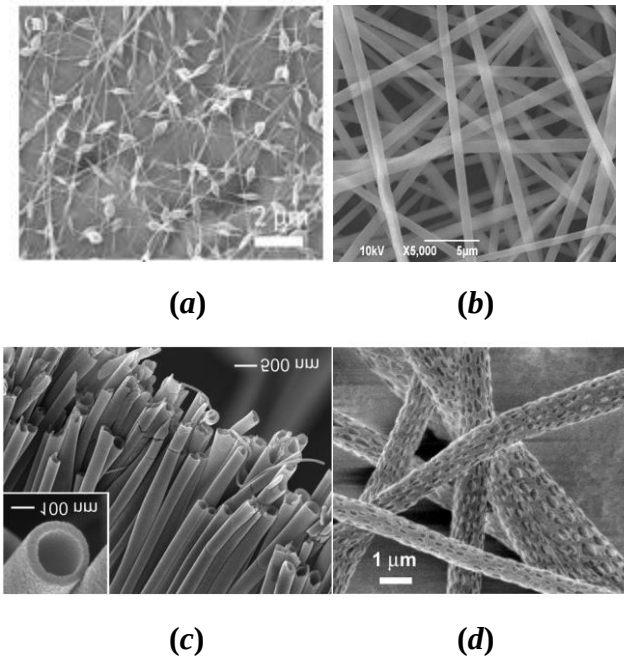

(*a*) (*b*)

(*c*) (*d*)

Figure 2.3: (*a*) Bead fiber (H. Fong et al., 1999); (*b*) Round fiber (Wu research Group); (*c*) Hollow fiber (Li & Xia, 2004); and (*d*) Porous fiber (Bognitzki et al., 2001).

Electrospun nanofibers have found many applications including nanocomposites, tissue engineering scaffolds, filtration devices, controlled drug release, sensors, energy conversion and storage, etc. (Greiner & Wendorff, 2007). In spite of their enormous potential applications, electrospun nanofibers have not been widely used in industry so far due mainly to the low productivity of electrospun nanofibers based on the conventional needle-based electrospinning technique. Needle-based electrospinning technique only allows for one jet initiation at a time, which results in the productivity typically much lower than any viable commercial use. The typical nanofiber productivity for needle-based electrospinning technique is only about 0.3g/hr. (Wang et al., 2012)

To improve the nanofiber productivity, low-cost, high-efficiency needleless electrospinning technique was developed as an alternative to the needle-based electrospinning technique. Needleless electrospinning is a novel electrospinning technique for massive production of ultrathin fibers, which is based on electrohydrodynamic jetting from the free

surface of a polymeric solution or melt. Multiple jets can be formed simultaneously from the needleless fiber generator. The self-organization process in needleless electrospinning is not as controlled as needle-based electrospinning, therefore, rational, robust models for needleless electrospinning process are highly desired for predictable massive fiber fabrication with tailorable fiber diameters and morphologies.

Extensive experimental investigation has been done on needleless electrospinning technique. Historically, Simm et al. (1979) first filed a patent to spin fibers. Simm et al. designed a ring spinneret for the electrostatic spinning of fiber fleece. It has taken nearly thirty years before needleless electrospinning began to show potential for the mass production of nanofibers. Jirsak et al. (2009) patented their needleless electrospinning technique, which utilizes a rotating cylinder as the spinneret for massive nanofiber production. This technique has been commercialized by Elmarco Inc. under the brand name Nanospider®. Many variations have been developed from the Nanospider® design. To mention a few, Wang et al. (2012) used a coil of wire as the spinneret for successful massive production of nanofibers. Niu et al. (2009) utilized a disc as the spinneret. Comparative study shows that each variation in the spinneret configuration results in a variation of the spun nanofibers. It has been observed that the geometry of the spinneret likely affects the properties of the electrospun nanofibers (Wang et al., 2012) . The spinneret used in needleless electrospinning has two influencing factors, i.e., the distribution of fiber production and the electric field in the working zone. An example of a rotating cylindrical spinneret (with dozen of ejecting jets) is shown in Figure 2.4.

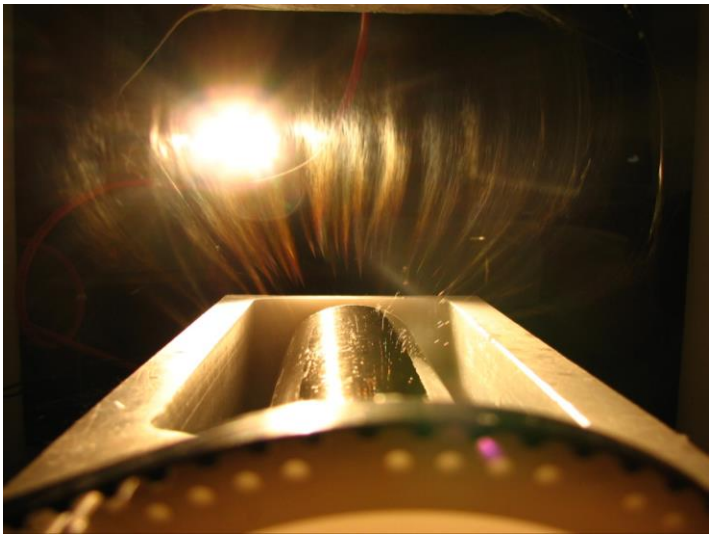

Figure 2.4: A rotating cylindrical spinneret with multiple jets. (Dr. Wu's research group at NDSU).

Other factors that affect the diameter of the fiber are the solution concentration (Shenoy et al., 2005), polymer molecular weight (Cengiz et al., 2010), surface tension, applied voltage (Li et al., 2014), dielectric constant (Luo et al, 2012), and ambient environment (e.g., temperature and humidity). When considering the effect of solution concentration, experimental study has shown that at the low polymer concentration, it typically resulted in fibers with beaded morphology instead of uniform, round fibers. In contrast, if the polymer concentration was too high, the high viscosity of the solution would resist stretching into fine filaments and fibers would not be formed (Shenoy et al., 2005). In addition, Niu et al. (2009) showed that within the range of acceptable solution concentrations for fiber generation, the solution concentration had a little effect on the fiber diameter.

Molecular weight of the polymer solvent in the solution is another significant factor in the fabrication process. Experimental study showed that polyvinyl alcohol (PVA) with a molecular weight less than 67,000 would be spinnable., PVA nanofibers can be electrospun in the PVA molecular weight of 80,000 to 150,000 (Cengiz et al., 2010).

Moreover, the dielectric constant of the solution has also a great effect on the diameter of the electrospun fibers. Luo et al. (2012) reported that fiber diameters less than 100 nm could be achieved when the relative dielectric constant was above 19. However, when the dielectric constant was below 19, the diameters of the electrospun fibers were in the range from sub-micrometer to millimeter (Luo et al, 2012).

Therefore, rational robust computational models capable of simulating multiple jets ejecting from free liquid surface are expected to take into account a majority of the factors that affect the diameter of the electrospun fibers. Such computational electrospinning models can at least take into account the solution concentration, surface tension, applied voltage, dielectric constant, and collecting distance, which would provide simulation results for experimental validation and scaling analysis of the material, process, and control parameters.

2.2. Current Understanding

Needleless nanofiber electrospinning is a multi-physics, electrohydrodynamic process for continuous, scalable nanofiber fabrication. The entire process of needleless electrospinning is extremely complex, involving electrohydrodynamic surface destabilization, multi-jet initiation, stretching, drying and solidification, and related phase transition and heat-mass transfer phenomena, among others. To date no theoretical and computational studies have been performed yet in the literature to model the fully three-dimensional (3D) process of needleless electrospinning. This study was focused on the initiation of multiple jets from a free liquid surface. This initial process for needleless electrospinning has also not been studied extensively due to the size scales and time limits involved in the jet initiation. To gain an insight into this complex process, a fabrication process was studied that resembles the phenomenon of needleless nanofiber electrospinning.

In a typical needleless electrospinning process, the formation of multi-jets from an open surface liquid follows this process: a flat layer of polymer solution is formed on the surface spinneret; small perturbation on the film causes the film to form into many cone like spikes; when the electric forces reach a critical value, cone-shaped structures form into “Taylor cones”; the jets are stretched out from the “Taylor cones”. Obviously, the study of other thin-film fabrication techniques would provide insight into how the structures on the surface of the spinneret form.

The use of electrohydrodynamic instabilities to pattern thin polymer films closely resembles the initial process of needleless electrospinning. Lithographically induced self-assembly (LISA), has been developed in the last two decades (Chou & Zhuang, 1999), which is an efficient, low-cost process for massive production of micro- and nano-scaled patterns on thin polymer films. The advantage of LISA technique is its one-step process with minimal equipment to pattern thin-film substrates. This technique can greatly reduce the cost of conventional photolithographic techniques employed in today’s microelectronics industry.

During a typical LISA process, a thin polymer film will be electrically deformed to self-assemble into micro or nanostructures under an unpatterned or patterned mask subject to a high DC voltage. A few examples of patterns produced using LISA technique are shown in Figure 2.5.

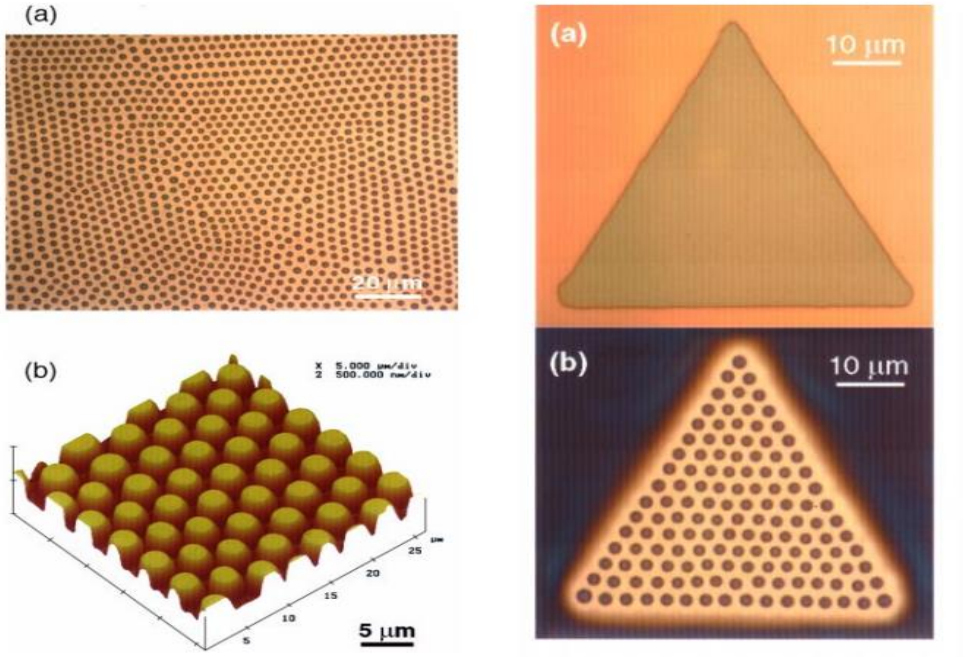

(*A*) **(*B*)**

Figure 2.5: (*A*) Micrographs of a pattern formation under an unpatterned mask. (*a*) Full optical micrograph, (*b*) AFM image. (*B*) Micrographs of a triangle pattern formation under a triangular patterned mask. (*a*) Triangle mask, (*b*) Pillar arrangement. (Chou & Zhuang, 1999).

In the LISA process, a thin polymer film is first spin-coated onto a flat solid substrate, heated above its glass transition temperature, and then annealed for a period of time in a high electrostatic field. Under these conditions, the properties of the polymer will allow the liquid film to replicate the patterned mask; upon cooling back to room temperature, the film will solidify into micro or nanostructure arrays.

Schäffer et al. (2000) explained the process by a balance of forces at the polymer-air interface. The surface tension of the polymer will try to minimize the surface area to stabilize the material, while the electrostatic force will polarize the polymer, causing an effective charge displacement at the interface, and destabilizing the material. This competitive process is usually explained in terms of pressure, i.e., the Laplace pressure competes with the electrostatic pressure

to reach the equilibrium state (Schäffer et al., 2001; Pease et al., 2002; Shankar et al., 2004; Wu et al., 2005). Initial small perturbations of the polymer-air interface is to simulate the environmental and material noises, which are responsible for generating a pressure gradient to drive the micro-patterning process. In the last two decades, both extensive experimental and theoretical studies have been performed to investigate the electrohydrodynamic destabilization of the patterning thin films (Chou et al., 1999; Schäffer et al., 2000; Chou et al., 2001; Lin et al., 2002; Wu et al., 2005). To date, numerous theoretical studies have shown that linear analysis of surface instability can be used for predicting the maximum growth rate and prediction of the final spacing between pillars; however, a fully dynamic simulation of the interface can only be realized by employing nonlinear analysis. So far, weakly nonlinear analysis has shown that the polymer film will self-organize into hexagonal arrays and the ratio of the polymer film thickness to the air gap is a dominate factor in determining the pattern that emerges from the process (Wu et al., 2003; Craster et al., 2005; Wu et al., 2005).

Fully 3D simulations can provide great insight into the formation of patterns on the surface of thin polymer melt. By using a phase field model and semi-implicit Fourier spectral method, Kim and Lu (2006) have shown the gorgeous dynamics of the system and proved that the formation of patterns is governed by the kinetic process as well as the energetics of the system. Wu et al. (2005) showed that the shape as well as the distance from the mask shapes the pattern that emerges. Li et al. (2014) proved that it is possible to fully replicate a patterned mask by controlling the solution parameters. It was shown that a polymer with a low surface tension and high dielectric constant is pliant to smaller spacing between neighboring pillars. It was also shown that viscosity of the material does not affect the overall pattern but helps with processing

time. The paper concluded that electrical voltage is the most significant variable in determining the outcome of the pattern (Li et al., 2014).

Numerous theoretical studies on electrohydrodynamic instabilities of patterning polymer films have shown the effect of choosing the correct numerical schemes as well as material parameters. The rich dynamics of this electrohydrodynamic process calls for a numerical algorithm that is both accurate and efficient. Kim and Lu (2006) and Wu et al. (2005) used a Fourier spectral method for spatial integration combined with a finite difference method for time integration to accurately and efficiently solve the PDEs involved in this process. The Fourier spectral method, unlike finite difference methods, makes use of global representation that results in a degree of accuracy that cannot be matched by local methods. This higher accuracy allows for a much coarser mesh that increases the efficiency of the method.

The Fourier spectral method works by transforming the system to the frequency domain from spatial domain by the use of a Fast Fourier Transform (FFT). The transformation decouples the differential equations and the resulting system of equations is solvable by algebraic means. The spectral methods were developed in a series of papers by Orszag (1977) to solve the rich dynamics involved with fluid mechanics.

2.3. Outstanding Problems in Electrohydrodynamic Instability Modelling

To date, considerable research has been conducted for predicting the patterning of thin films due to electrohydrodynamic instabilities. These works, while significant, fail to capture the full potential of the model by either assumption or striving too much for efficiency. The present work will try to improve upon existing models to capture the full potential of this model.

The use of current electrolithography models to gain insight into modelling the initiation of multiple jets from a free liquid surface is significantly helpful, but the self-assembly process

taking place in electrolithography, while similar, is significantly different from the needleless electrospinning process. The current models for thin polymer film patterning make assumptions that could be detrimental to the accuracy of the models. Wu et al. (2005) showed great accuracy in tracking the morphology of the air-polymer interface by using a Fourier spectral method, but they made assumptions about the surface tension while also claiming that the surface tension is paramount to the entire process. The use of the small angle approximation to reduce the curvature formula to calculate the surface tension of a free liquid surface can greatly improve the efficiency of computational simulations, but the reduced curvature model may fail to capture the small features and reduce the surface tension that guides the pattern to emerge from the polymer melt. Since fiber generation from a free liquid surface can only happen under certain conditions the small features need to be accurately modeled for predicting the real world application. In Chapter 3 the electrolithography models developed by Wu et al. (2005) and others will be modified to incorporate the exact curvature of the surface that will not reduce the surface tension in order to more precisely capture the small features of the surface morphology. This modification, in conjunction with a highly efficient finite-difference-Fourier-spectral method will greatly enhance the model capability of accurately predicting the patterning in thin films.

The second major difference between the electrolithography process and the needleless electrospinning process is the existence of a volatile solvent in the polymer solution. The electrolithography process calls for the use of a polymer melt without a solvent. Solvent is needed to decrease viscosity in the needleless electrospinning process and also affects the dielectric constant of the material (Luo et al., 2012). The polymer solution made of a volatile solvent and a stable polymer will experience a varying viscosity due to drying that will affect the final morphology of the air-polymer interface (Schwartz et al., 2001). The existing models for

electrohydrodynamic surface patterning fail to capture the dual phase properties of the polymer solution in needleless electrospinning. Chapter 4 will formulate a solvent-evaporation-involved electrohydrodynamics model and related FFT-based spectral method for capturing the multi-jet initiation in needleless electrospinning process.

Chapter 5 will summarize the current research and expect the future work following the present thesis work.

3. COMPUTATIONAL SIMULATIONS OF SURFACE PATTERNING IN ELECTROLITHOGRAPHY

3.1. Introduction

In this chapter, a robust, high-efficiency computational model is formulated for accurately capturing the electrohydrodynamic evolution of the surface morphology of thin polymer melts subjected to electrostatic field. The proposed model adopts the exact expressions of the physical terms in the governing PDEs and therefore is capable of providing more accurate predictions than those of existing models in the literature, especially the small features of the surface-patterning films. To accurately solve the resulting governing PDE of the model, a high-efficiency finite-difference Fourier-spectral method is formulated, and related compact computer codes are designed to implement the present computational model. The temporal evolution of the surface morphology predicted by the proposed model is validated by the existing models in the literature (Craster & Matar, 2005; Shankar & Sharma, 2004; Verma et al., 2005; Wu & Chou, 2003; Yang et al., 2013; Li et al., 2014). The present predictive model can be utilized for controllable production of electrohydrodynamically patterned thin polymer films.

The polymer considered in the present modeling is assumed viscous, incompressible fluid. Figure 3.1 shows the schematic setup of a typical electrolithographic process, which is similar to the needleless electrospinning process. The top electrode is positioned with a distance H ($H >> h$, h is the film thickness) above the surface of the thin film. If a patterned mask is introduced, it will be attached onto the top electrode. The distance from the top electrode to the mask surface is designated with variable h_{m}. The height of the film surface is measured as the distance from the bottom electrode and designated by variable h. The notation and formulation

are closely related to those discussed in the literature (Craster & Matar, 2005; Shankar & Sharma, 2004; Verma et al., 2005; Wu & Chou, 2003; Yang et al., 2013; Li et al., 2014).

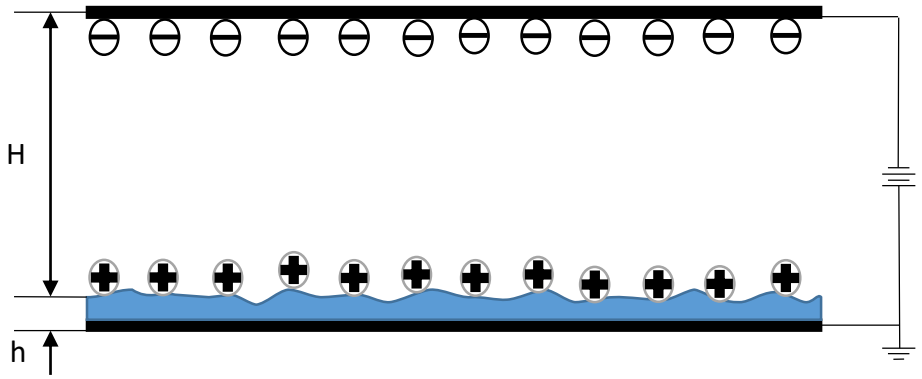

Figure 3.1: Schematic experimental setup of electrolithography process.

3.2. Problem Formulation

To begin, a thin polymer film is spin-coated on a solid substrate with a high surface energy. This thin polymer film experiences a homogeneous electrostatic field and carries a low Reynolds number during its evolution. The low Reynolds number guarantees that the inertial effects of the film can be ignored. Thus, the governing PDEs of the thin film are the continuity and Navier-Stokes (creeping fluid) equations:

$$\nabla \bullet \vec{j} + \frac{\partial h}{\partial t} = 0, \tag{3.1}$$

$$-\nabla p + \mu \nabla^2 \vec{v} = 0. \tag{3.2}$$

In the above, $\vec{j}$ is the pressure-driven flux in the polymer film, h is the height of the film surface above the substrate, $\vec{v}$ is the velocity field of the fluid, p is the pressure in the fluid, and μ is the viscosity of the fluid. The fluid velocity field satisfies the no-slip conditions at both the top and bottom electrodes. In addition, the liquid film is assumed to be incompressible:

$$\nabla \bullet \vec{v} = 0. \tag{3.3}$$

By using the lubrication approximation and Eq. (3.2), the pressure-driven flux $\vec{j}$ can be related to the gradient of the film pressure p as

$$\vec{j} = \frac{h^3}{3}(-\nabla p). \tag{3.4}$$

Substitution of Eq. (3.4) into Eq. (3.1) yields the nonlinear kinematic equation of the thin film (Craster & Matar, 2005; Shankar & Sharma, 2004; Verma et al., 2005; Wu & Chou, 2003; Yang et al., 2013; Li et al., 2014; Schaffer et al., 2000):

$$\frac{\partial h}{\partial t} = \frac{h^3}{3}\nabla^2 p. \tag{3.5}$$

As mentioned in the literature review in Chapter 2, multi-jets and pillars initiated from the free surface of the thin polymer film are resulted from the competition between two types of forces, i.e., the electrostatic force and the capillary pressure due to surface tension of the film. The electrostatic field is to polarize the polymer and cause it to rise, and the surface tension is to minimize the surface area of the film. These two types of forces determine the evolution of the surface patterning to minimize the global free energy of the system. To model this type of electrohydrodynamic phenomenon, the driving pressure of the thin-film system should be determined, which consists of three terms, i.e., the electrostatic pressure, p_e, the Laplace pressure, p_s, and the disjoining pressure, p_{dis}. Herein, the disjoining pressure is introduced to satisfy the no-penetration condition at the top and bottom electrode in the case of LISA. Thus, the total pressure of the system is:

$$p = p_o - p_s - p_e - p_{dis}, \tag{3.6}$$

where p_o is the atmospheric pressure, assumed to constant in most simulations.

The electrostatic pressure p_e is determined as (Verma et al., 2005):

$$p_e = -\frac{1}{2}\varepsilon_0(E_a^2 - \varepsilon E^2), \tag{3.7}$$

where E_a represents the electrostatic field in the air phase, E represents the electrostatic field in the polymer phase, ε_0 is the permittivity of free space, and ε is the dielectric constant of the polymer film. The electrostatic field is irrotational and solenoidal. The electric field of the air phase and the polymer phase is determined by solving the Laplace equation for electric potential, i.e. $\nabla^2\psi = 0$. To solve the Laplace equation for this problem set up, the Laplace equation is broken down into two governing equations represented by Eq. (3.8):

$$\frac{\partial^2\psi_p}{\partial z^2} = 0; \qquad \frac{\partial^2\psi_a}{\partial z^2} = 0 \tag{3.8}$$

with subscripts *a* and *p* representing the air and polymer phases, respectively. The boundary conditions (BCs) used to solve for the electrostatic pressure p_e are:

$$\begin{cases} \psi_a = 0, & (z = d = H - h_m) \\ \dfrac{\partial\psi_a}{\partial x}\varepsilon_a = \varepsilon_p \dfrac{\partial\psi_p}{\partial x}, & (z = h) \\ \psi_p = U. & (z = 0) \end{cases} \tag{3.9}$$

In the above, U is the applied voltage between two electrodes, and d is the height of the top electrode. Solving Eq. (3.9) results in the electrostatic potential between the two electrodes as

$$\begin{cases} \psi_a = \dfrac{U\varepsilon_p(z-d)}{d\varepsilon_p - h(\varepsilon_p - 1)}, \\ \psi_p = U\left[1 + \dfrac{z}{\varepsilon_p d - h(\varepsilon_p - 1)}\right]. \end{cases} \tag{3.10}$$

The electric fields for the polymer and air phases can be determined from expression (3.10) as

$$\begin{cases} E_{zp} = -\dfrac{\partial \psi_p}{\partial z} = \dfrac{-U}{\varepsilon_p d - h(\varepsilon_p - 1)}, \\ E_{za} = -\dfrac{\partial \psi_a}{\partial z} = \dfrac{-U\varepsilon_p}{\varepsilon_p d - h(\varepsilon_p - 1).} \end{cases} \tag{3.11}$$

Plugging the electric field (3.11) into Eq. (3.7) leads to the electrostatic pressure p_e of the thin polymer film as

$$p_e = \frac{-U^2 \varepsilon_0 (\varepsilon - 1)\varepsilon}{2[h + (H - h_m - h)\varepsilon]^2}. \tag{3.12}$$

The Laplace pressure p_s is determined by the Young-Laplace equation:

$$p_s = \gamma \nabla^2 h, \tag{3.13}$$

where γ represents the value of the surface tension, and $\nabla^2 h$ stands for the linearized curvature of the surface for small slopes.

Herein, the Laplace pressure p_s is the pressure difference between the inside and outside of a curved surface, which is caused by the surface tension of the boundary between the air and polymer phases. The operator ∇^2 stands for the Laplace operator in two-dimensions (2D) and is defined by $\nabla^2 h = \Delta h = \dfrac{\partial^2 h}{\partial x^2} + \dfrac{\partial^2 h}{\partial y^2}$.

The disjoining pressure p_{dis} is defined as (Wu et al., 2005):

$$p_{\text{dis}} = \frac{A}{(H - h_m - h)^3} - \frac{A}{h^3}, \tag{3.14}$$

where A is the effective Hamaker constant. The disjoining pressure p_{dis} is the pressure caused by the van der Waal forces in thin films in close approach to the electrodes. The disjoining pressure, p_{dis}, arises from the attraction or repulsion of two surfaces. This pressure represents how the fluid interacts with the electrodes. These two terms in the disjoining pressure in (3.14) are used to

force the stability at the two electrodes and to satisfy the no-penetration condition. The first term of Eq. (3.14) represents the disjoining pressure p_{dis} at the top electrode while the second term represents that at the bottom electrode. The right term is to force the governing equation to fully wet the surface of the bottom electrode by having the maxima as the thickness of the film tends to zero. The introduction of the disjoining pressure p_{dis} at the top and bottom electrodes keeps the surface of the thin film away from the electrodes. Physically, the disjoining pressure p_{dis} represents the intermolecular interactions at interfaces.

Plugging the electrostatic pressure p_e (Eq. 3.12), Laplace pressure p_s (Eq. 3.13), and the disjoining pressure p_{dis} (Eq. 3.14) into Eq. (3.6) leads to the global driving pressure of the system (Wu et al., 2005):

$$p = -\frac{U^2\varepsilon_0(\varepsilon-1)\varepsilon}{2[h+(H-h_m-h)\varepsilon]^2} - \gamma\nabla^2 h + [\frac{A}{(H-h_m-h)^3} - \frac{A}{h^3}]. \tag{3.15}$$

To simplify the simulation process, the model is further normalized in a dimensionless way as follows. To begin the process, Eq. (3.15) is first multiplied by the length scale L:

$$pL^2 = -\frac{L^2U^2\varepsilon_0(\varepsilon-1)\varepsilon}{2[h+(H-h_m-h)\varepsilon]^2} - \gamma h + L^2[\frac{A}{(H-h_m-h)^3} - \frac{A}{h^3}]. \tag{3.16}$$

The next step is to divide the terms in Eq. (3.16) by the term γH:

$$\frac{pL^2}{\gamma H} = -\frac{U^2\varepsilon_0(\varepsilon-1)\varepsilon}{\gamma H 2[h+(H-h_m-h)\varepsilon]^2} + \frac{L^2}{\gamma H}[\frac{A}{(H-h_m-h)^3} - \frac{A}{h^3}]. \tag{3.17}$$

Herein, the characteristic length scale L is defined by

$$L^2 = \frac{\gamma H}{U^2\varepsilon_o}. \tag{3.18}$$

Furthermore, a term $H^3$is multiplied to the terms at both sides of Eq. (3.17):

$$\frac{pH^3}{U^2\varepsilon_o} = -\frac{H^3(\varepsilon-1)\varepsilon}{2[h+(H-h_m-h)\varepsilon]^2} + \frac{A}{U^2\varepsilon_o}. \tag{3.19}$$

Finally, the dimensionless parameters and variables of the model are listed in expression (3.20):

$$\begin{aligned} &\bar{h} = \frac{h}{H}, \quad \bar{h}_0 = \frac{h_0}{H}, \quad \bar{h}_m = \frac{h_m}{H}, \\ &\bar{p} = \frac{pH^2}{U^2\varepsilon_0}, \quad \bar{A} = \frac{A}{HU^2\varepsilon_0}. \end{aligned} \tag{3.20}$$

For the convenience of expression, the symbol bar is ignored in the upcoming equations. Therefore, the dimensionless driving pressure of system is

$$p = -\frac{(\varepsilon-1)\varepsilon}{2[h+(1-h_m-h)\varepsilon]^2} - \nabla^2 h + [\frac{A}{(1-h_m-h)^3} - \frac{A}{h^3}]. \tag{3.21}$$

These dimensionless terms have been adopted in the literature (Wu et al., 2005). The next step is to make the evolution Eq. (3.5) dimensionless. The process is the same and the characteristic time scale *T* is found to be

$$T = \frac{H^3\mu\gamma}{(\varepsilon_o U^2)^2}. \tag{3.22}$$

After introducing the dimensionless model parameters and variables, the dimensionless kinetic equation governing the pattern evolution in thin polymer films is

$$\frac{\partial h}{\partial t} = \nabla\bullet(\frac{1}{3}h^3\nabla p), \tag{3.23}$$

where

$$p = -\frac{(\varepsilon-1)\varepsilon}{2[h+(1-h_m-h)\varepsilon]^2} - \nabla^2 h + [\frac{A}{(1-h_m-h)^3} - \frac{A}{h^3}]. \tag{3.24}$$

Eqs. (3.23) and (3.24) will be solved numerically to obtain the height evolution of a thin polymer film. This model is capable of accurately recreating the patterns reported in the literature. This model is relatively simple but is able to provide accurate results for slow moving,

long-wave instabilities in single phase polymer melts. Yet, additional efforts are still needed in order to formulate an accurate rational model for needleless electrospinning.

In order to enhance the accuracy of the above model prediction, the exact expression of the Laplace pressure, p_s is used to replace expression (3.13). Herein, the Laplace pressure p_s plays a significant role in the evolution of the surface pattern in the polymer films. As aforementioned, the competition between the Laplace pressure p_s, to stabilize the fluid and the electrostatic pressure p_e, to destabilize the fluid, causes the unique pattern evolution. As a matter of the fact, the linearization of the curvature formula used in the Laplace pressure p_s of the literature models actually allows the polymer films to grow unstable with less predictive accuracy by comparison with that based on the exact curvature formula under consideration. In this study, the curvature formula used in Eq. (3.13) will be replaced by the exact mean curvature formula

$$H = \frac{1}{2}\left(\frac{1}{\rho_1} + \frac{1}{\rho_2}\right) = \frac{(1+h_x^2)h_{yy} - 2h_x h_y h_{xy} + (1+h_y^2)h_{xx}}{(1+h_x^2+h_y^2)^{\frac{3}{2}}}. \tag{3.25}$$

The choice to exclude the small-angle approximation and use the exact curvature formula in one-dimensional (1D) modeling of LISA process has been considered in the literature (Wu & Chou, 2003). This chapter will consider the general 2D case for modeling the surface patterning in polymer films. In Section 3 of this chapter, an efficient finite-difference Fourier-spectral method will be formulated to solve the kinetic equation of the thin films for simulating the temporal surface patterning process. Comparison between thin-film models based on linearized and exact curvature formulas will be made in Section 4 of this chapter.

3.3. Numerical Scheme

To fully capture the unique features of thin film evolution, formulation of an accurate and efficient numerical method is crucial. In this section an efficient finite-difference Fourier-spectral method is formulated to solve the governing PDE developed in the previous section. This section will show step-by-step how to implement the finite-difference Fourier-spectral method and develop a flow chart in solving for the evolving PDE of the surface morphology.

As explained in Chapter 2, the Fourier spectral method for spatial integration combined with the finite difference method for time integration will accurately and efficiently solve the PDE governing this surface-patterning process. The Fourier spectral method, unlike finite difference methods, makes use of global representation that results in a degree of accuracy that cannot be matched by local methods. This higher accuracy allows for a much coarser mesh that increases the efficiency of the method.

The Fourier spectral method works by transforming the system to the frequency domain from spatial domain by evoking the FFT. The transformation decouples the differential equations, and the resulting system of equations is solvable by algebraic means. The spectral methods were developed in a series of papers by Steven Orszag (1977) to solve the rich dynamics involved in fluid mechanics.

For the time integration, first-order finite difference method will be employed to reduce the complexity of the numerical scheme. When the first-order finite difference method is applied, the discretized form is obtained:

$$\frac{\partial h}{\partial t} = \frac{h^{n+1} + h^{n}}{\Delta t}, \tag{3.26}$$

where Δt is the dimensionless time step for the iteration.

Applying the first-order finite difference method to the evolution Eq. (3.23) and solving for h^{n+1} will give the updated surface morphology:

$$h^{n+1} = \Delta t(\nabla\bullet(\frac{1}{3}(h^n)^3\nabla p^n) + h^n. \tag{3.27}$$

The next step in solving for the updated surface morphology is applying the Fourier spectral method for spatial integration. An example of how the Fourier spectral method is applied is shown as

$$\nabla^2 Y + M\nabla Y \rightarrow k^2\hat{Y} + [M(k\hat{Y})_r]_k. \tag{3.28}$$

The caret or subscript *k* stands for the Fourier transform. The vector ***k*** is the wave number in Fourier space, and $k^2 = k_x^2 + k_y^2$. The subscript *r* stands for the inverse Fourier transform. All the discrete Fourier transform and its inverse can be performed efficiently and accurately by adopting the FFT. The following equations will adhere to the same notation as used in the example. Each spatial derivative will be solved for in Fourier space to decouple it and turn the whole into a system of equations.

To begin, each term of the pressure equation needs to be solved. The Laplace pressure p_s in Eq. (3.25) is the first term of the pressure, which is solved by using the Fourier spectral method. The exact Laplace pressure p_s, can be expressed as

$$p_s = 2\gamma H = 2\gamma\frac{h_{xx}h_y^2 - 2h_{xy}h_xh_y + h_{yy}h_x^2}{\left(1+h_x^2+h_y^2\right)^{\frac{3}{2}}}, \tag{3.29}$$

where subscripts *x* and *y* stand for the derivative with respect to the spatial direction *x* and *y*, respectively.

If each derivative in the Laplace pressure p_s were solved by a finite difference method, the numerical accuracy would be very low and the computer code would also be huge and

unwieldy. Adoption of the FFT allows an easy implementation of the Fourier spectral method. As a result, the exact Laplace pressure p_s can be solved in Fourier space by means of the Fourier spectral method as

$$p_{lap} = 2\gamma H = 2\gamma \frac{\left(-k_x^2 \hat{h}\right)_r \left(ik_y \hat{h}\right)_r^2 - 2\left(-k_y k_x \hat{h}\right)_r \left(ik_x \hat{h}\right)_r \left(ik_y \hat{h}\right)_r + \left(-k_y k_y \hat{h}\right)_r \left(ik_x \hat{h}\right)_r^2}{\left(1 + \left(ik_x \hat{h}\right)_r^2 + \left(ik_y \hat{h}\right)_r^2\right)^{\frac{3}{2}}}. \quad (3.30)$$

In the above, each caret or subscript *k* stands for the Fourier transform, and each subscript *r* stands for an inverse Fourier transform. Each spatial derivative in Eq. (3.29) is solved in Fourier space by evoking the FFT and returning to the physical space using inverse FFT. Once the Laplace pressure p_s is solved, it can be used to solve for the total pressure *p* of the system in physical space such that

$$p = \frac{-(\varepsilon - 1)\varepsilon}{2[h + (1 - h_m - h)\varepsilon]^2} - 2\gamma H + [\frac{A}{(1 - h_m - h)^3} - \frac{A}{h^3}]. \quad (3.31)$$

Once the total pressure *p* is solved for the system, it can be plugged into Eq. (3.27) to solve for the updated surface morphology. Define an intermediate function in the Fourier domain at time step *n*, which is used for the next numerical iteration for determining the surface morphology at time step *n*+1:

$$\hat{f}^n = [\frac{1}{3}(h^n)^3(-k^2 \hat{p}^n)_r]_k + \{\frac{1}{3}(h^n)^2[(ik_x \hat{p}^n)_r (ik_x \hat{h}^n)_r + (ik_y \hat{p}^n)_r (ik_y \hat{h}^n)_r]\}_k . . \quad (3.32)$$

Once expression (3.32) is evaluated, the height of the thin film (morphology) at time step *n*+1 can be determined as

$$\hat{h}^{n+1} = \Delta t(\hat{f}^n) + \hat{h}^n. \quad (3.33)$$

When the updated surface morphology in Fourier space is solved, the surface morphology is updated in physical space by the use of the inverse FFT.

The numerical iteration for solving the governing kinetic equation of the thin films can be expressed in term of a flow chart as shown in Fig 3.2.

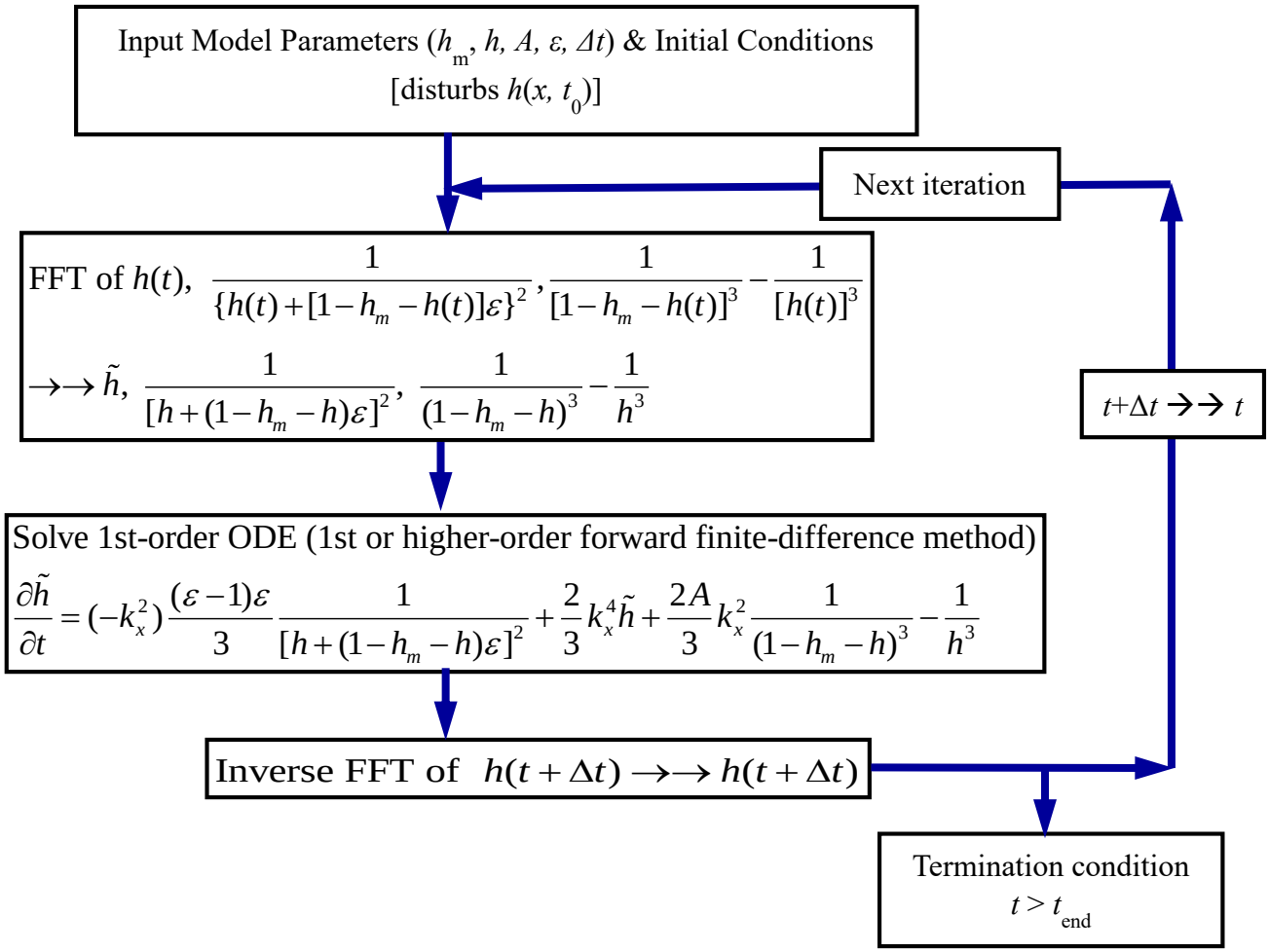

Figure 3.2: Flow chart of the numerical procedure for solving the surface morphology of thin polymer films.

The flow chart follows the procedure as used in implementing the numerical scheme in Matlab®.

The numerical iteration outlined in the flow chart follows:

- Input all the model parameters and initial conditions.
- Convert the height of the film, electrostatic pressure and disjoining pressure into Fourier space using the FFT
- Solve for the total pressure of the system and input into Eq. (3.32)
- Update the surface morphology in physical space by use of the IFFT

3.4. Results and Discussion

This section is to show the numerical results for a series of simulations based on the models formulated in Section 3.2. To start off, the model was first reduced to a 1D model for the convenience of validation and testing. The 1D model provides a simple model for initial observations and comparison. The 1D model was run with a dimensionless time step of dt = 0.001128 grid nodes, an initial film height following a cosine distribution centering on 0.7, and a dimensionless Hamaker constant $A = 2.26 \times 10^{-5}$. Figure 3.3 shows the results for the 1D model over time. Figure 3.4 shows the results for the reduced 1D model with linearized curvature formula.

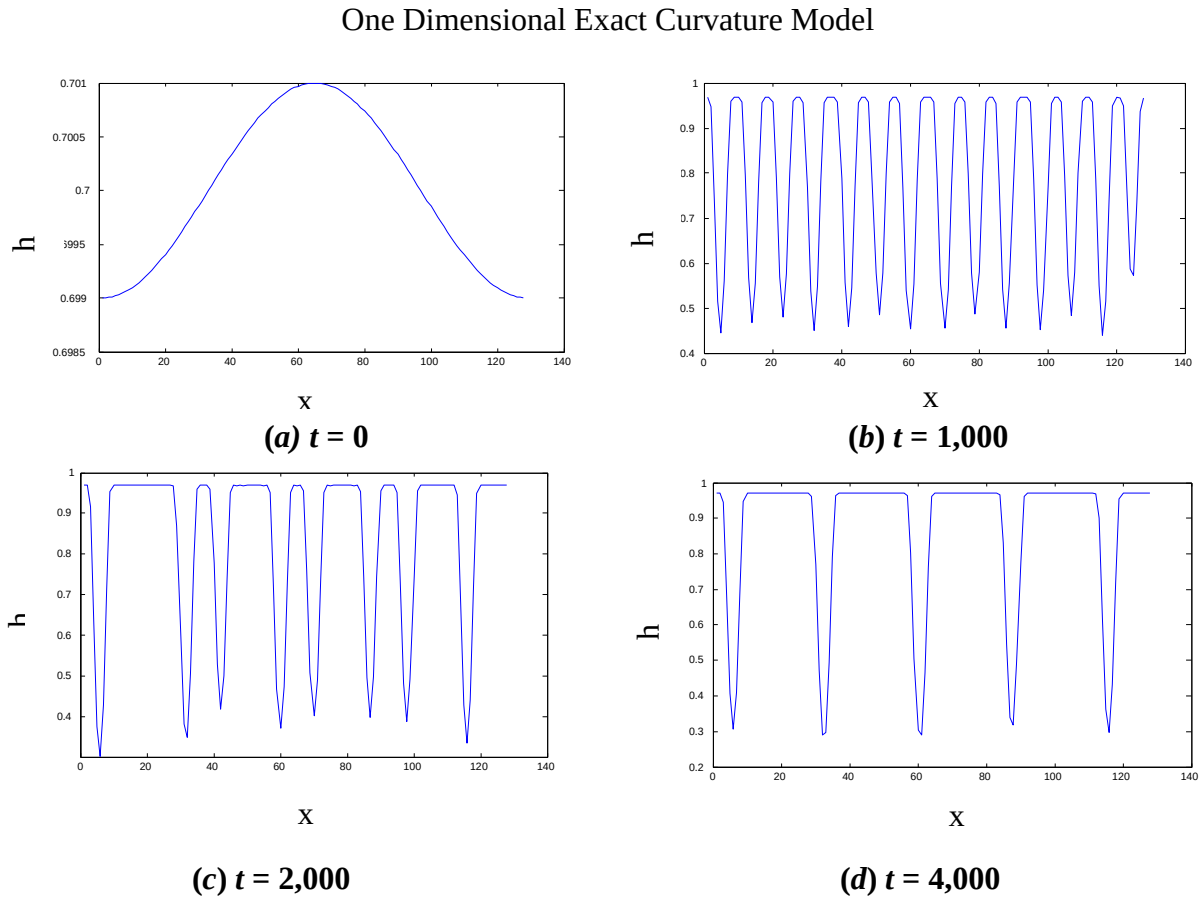

Figure 3.3: 1D surface morphology of polymer thin films at dimensionless time steps: (*a*) *t* = 0, (*b*) *t* = 1,000, and (*c*) *t* = 2,000, and (*d*) *t* = 4,000.

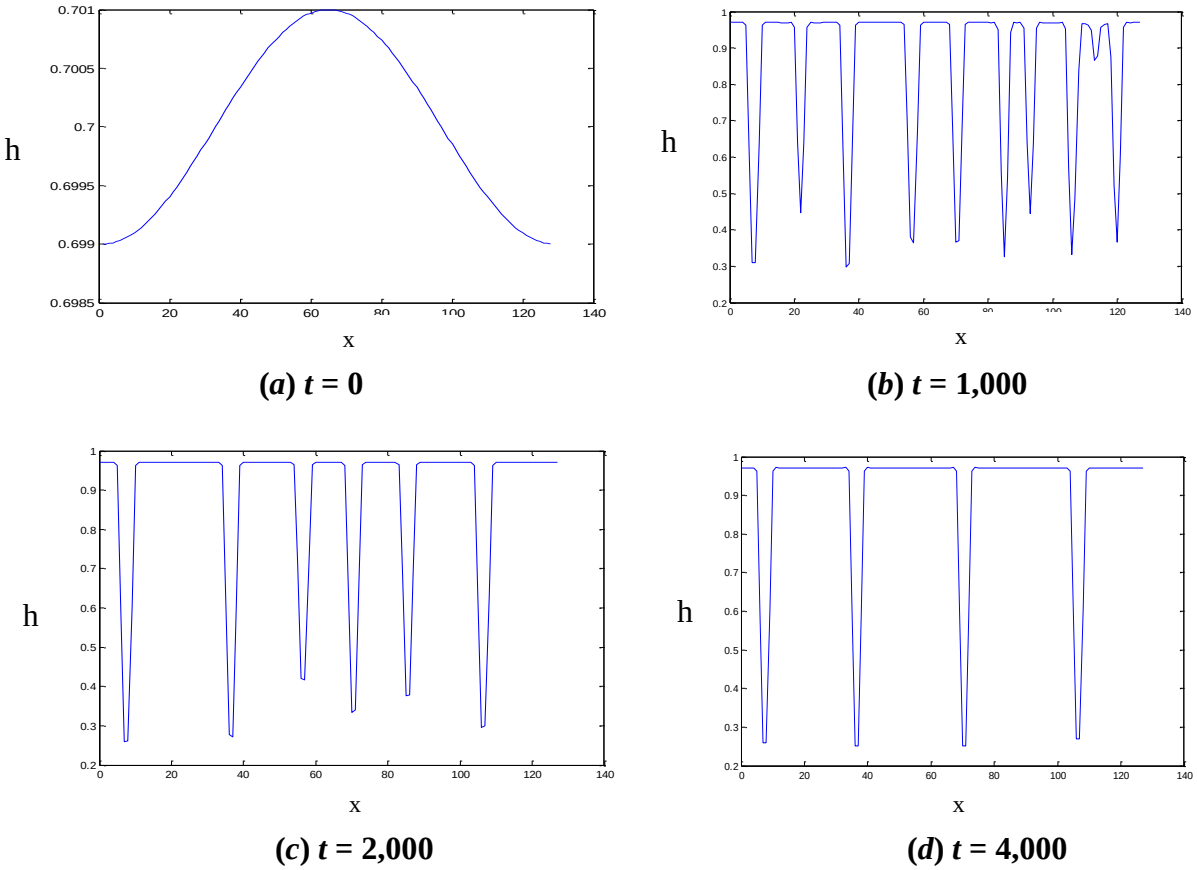

(*a*) *t* = 0 **(*b*) *t* = 1,000**

(*c*) *t* = 2,000 **(*d*) *t* = 4,000**

Figure 3.4: 1D surface morphology of polymer thin films at dimensionless time steps: (*a*) *t* = 0, (*b*) *t* = 1,000, (*c*) *t* = 2,000, and (*d*) *t* = 4,000.

The thin polymer melt starts with the distribution as shown in Fig. 3.3 (*a*). It will reorder itself in order to minimize its surface energy. It first does this by spreading out, and this results in a flatter distribution than its original configuration as shown in Fig. 3.3 (*a*). By the time step reaches 1,000, the material has grown unstable due to the electric field. Small columns have started to initiate. This shape is the most stable one that the polymer can reach at this point. As the time step continues, the polymer columns have started to coalesce to form wider columns. As the time step reaches the high numbers, the polymer has reached a minimum energy level and forms symmetric columns. This entire process is governed by the competition between the surface pressure and the electrostatic pressure. Figure 3.5 shows the corresponding evolution of

the surface energy. The formulation for the energy is shown below (Wu et al., 2005), with *Surf*, *VDW*, and *ELEC* standing for the surface energy related to the surface tension, van der Waal forces, and electrostatic forces, respectively.

$$Energy = Surf + VDW + ELEC \tag{3.34}$$

$$\begin{cases} Surf = \int_0^l \gamma \sqrt{1+\left(\frac{dh}{dx}\right)^2}\, dx, \\ VDW = \int_0^l \left[\int_h^\infty \frac{A}{h^3} dh + \int_{1-h}^\infty \frac{A}{(1-h)^3} d(1-h) \right] dx, \\ ELEC = -\int_0^l \frac{\varepsilon\varepsilon_0}{2\left[h+\varepsilon(1-h)\right]} dx. \end{cases} \tag{3.35}$$

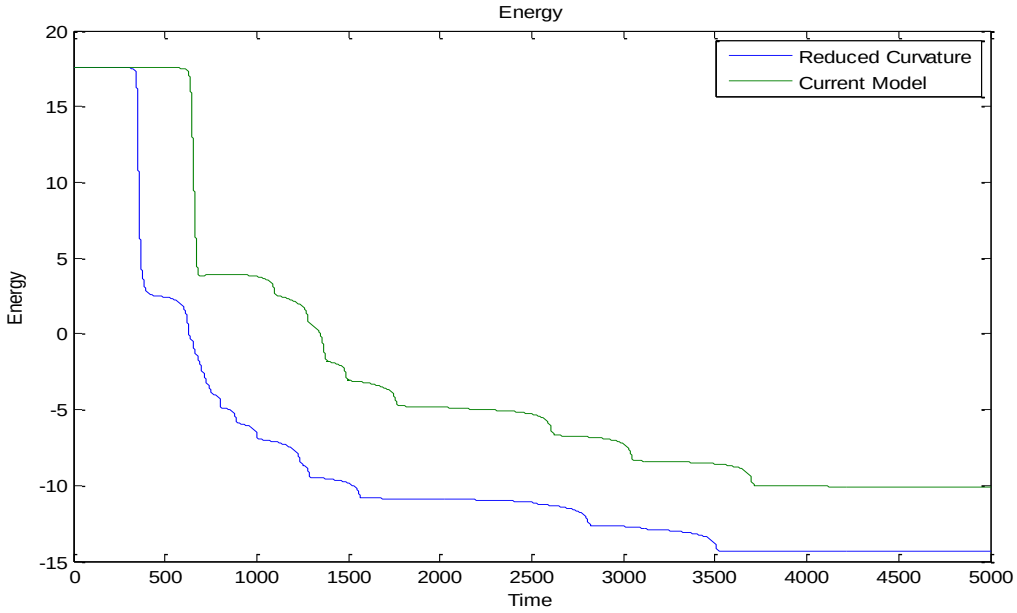

Figure 3.5: Energies of the system based on two curvature models.

Figure 3.4 shows the entire energy of the system over time based on the simulations using two different models, i.e., the present model with the exact curvature formula and the reduced model with the linearized curvature formulas in Section 3.2. The long flat regions as shown in the figure represent the semi-stable distributions of the polymer surface. Notice the difference in the energy over time between the two different models. Given the same time steps for the

numerical iterations, the current curvature model has more semi-stable regions and thus has a higher lowest energy than that predicted by the reduced curvature model. This information means that the current curvature models is more stable over time than the reduced curvature model, and it will take longer time to reach a final stage of evolution.

Figure 3.6 shows a comparison between the 3D reduced curvature and current models developed in Section 3.2. The initial height of the film was $h_0 = 0.49$, mesh size was 64 × 64, dielectric constant was ε = 3.5, Hamaker constant $A = 2.26 \times 10^{-5}$, and $dt = 0.00075$.

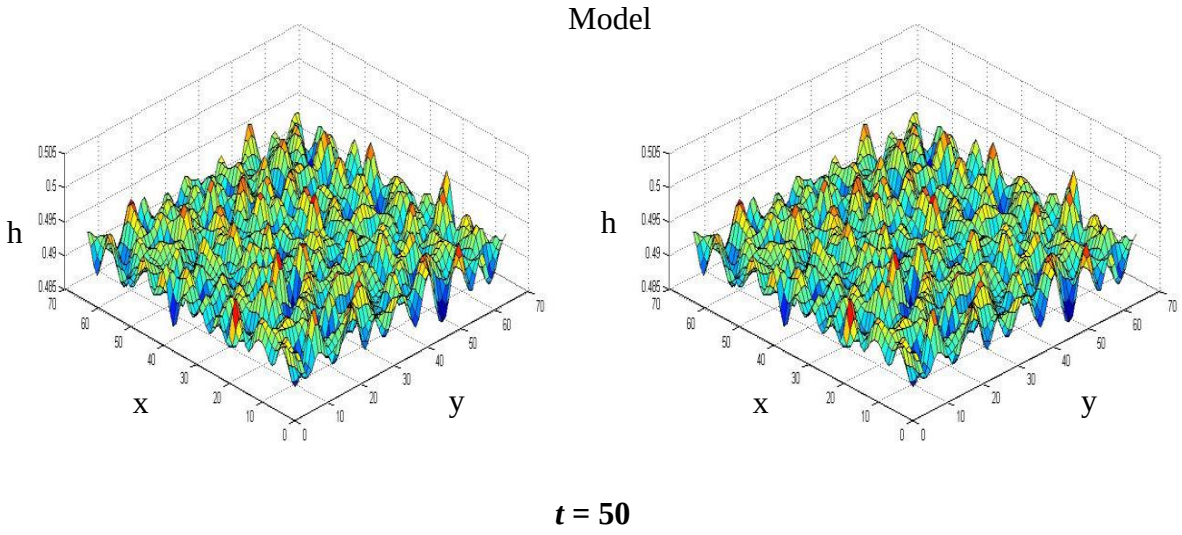

Figure 3.6: Comparison of the surface morphology of the thin films using two different curvature models in the range of dimensionless time step from 50 to 200. The left-side panels show the results of the reduced curvature model; the right-side panels show the results of the non-reduced curvature model. (The initial height of the film: $h_0 = 0.49$ with random initial surface perturbation of the amplitude 0.005, mesh size: 64 × 64, dielectric constant: ε = 3.5, Hamaker constant $A = 2.26 \times 10^{-5}$ and $dt = 7.5 \times 10^{-4}$).

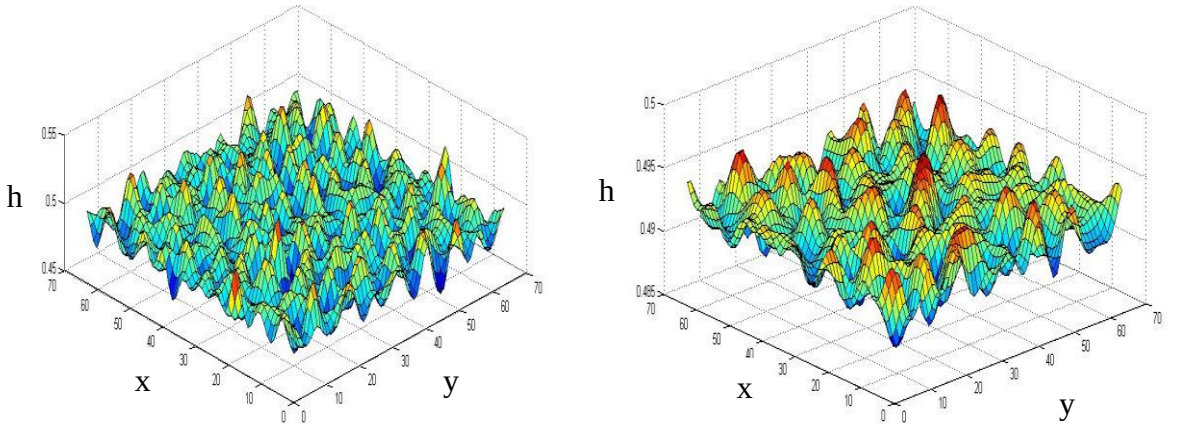

***t* = 100**

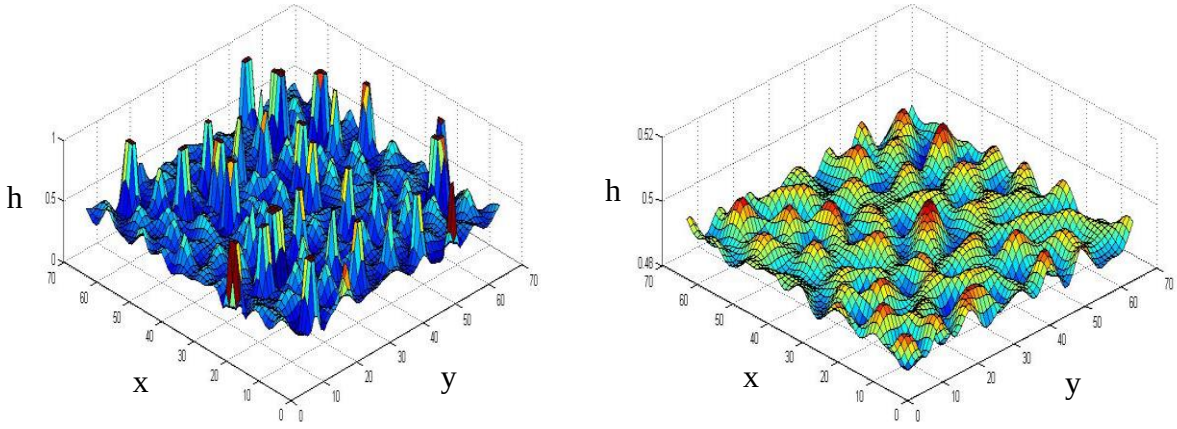

***t* = 150**

Figure 3.6: Comparison of the surface morphology of the thin films using two different curvature models in the range of dimensionless time step from 50 to 200 (continued). The left-side panels show the results of the reduced curvature model; the right-side panels show the results of the non-reduced curvature model. (The initial height of the film: h_0 = 0.49 with random initial surface perturbation of the amplitude 0.005, mesh size: 64 × 64, dielectric constant: ε = 3.5, Hamaker constant $A = 2.26 \times 10^{-5}$ and $dt = 7.5 \times 10^{-4}$).

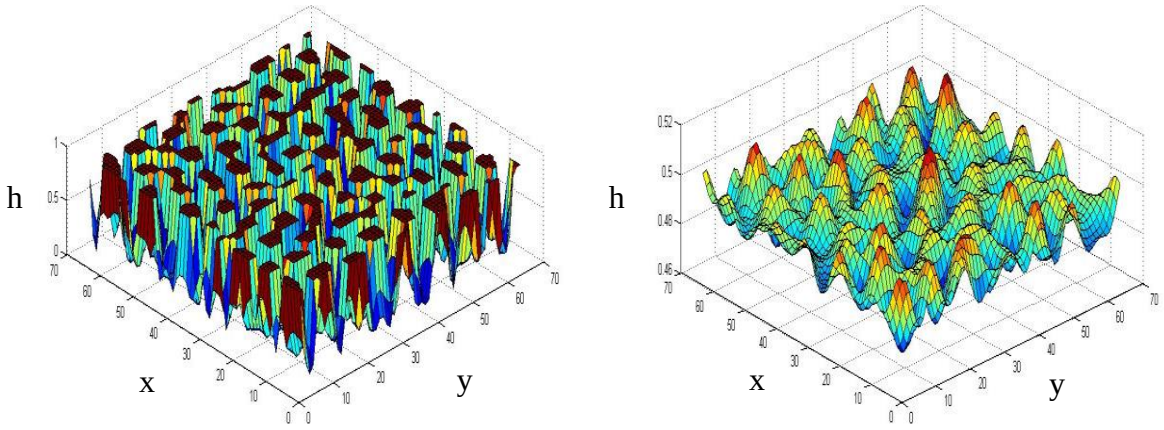

***t* = 200**

Figure 3.6: Comparison of the surface morphology of the thin films using two different curvature models in the range of dimensionless time step from 50 to 200 (continued). The left-side panels show the results of the reduced curvature model; the right-side panels show the results of the non-reduced curvature model. (The initial height of the film: h_0 = 0.49 with random initial surface perturbation of the amplitude 0.005, mesh size: 64 × 64, dielectric constant: ε = 3.5, Hamaker constant $A = 2.26 \times 10^{-5}$ and $dt = 7.5 \times 10^{-4}$).

The 3D plots on the left-side of Fig. 3.6 show the results based on the reduced curvature model. This model has the growth rate faster than that of the current curvature model. This means that the reduced curvature model leads to a less stable surface than that of the current model. Such a fast growth could cause worse predictions of the model that do not coincide with experimental observations. In the present study, the initial height for both models was $h_0 = 0.49$ and the dielectric constant was ε = 3.5. When the electrostatic field was first applied, the surface undulation was expected to grow over time. At $t = 50$ in both models, the electrostatic pressure had begun to overcome the surface tension of the polymer and pulled the interface upward. At $t = 100$, a noticeable difference started to emerge between the two models. The film surface predicted by the reduced curvature surface was further pulled upward and cones, arranged in a periodic pattern, started to emerge on the surface. In contrast, the film surface predicted by the current curvature model remained unchanged. As time progressed, the cones continued to grow

and started to form pillars due to the interaction with the top electrode. The film surface predicted by the current curvature model just started to form more cone-like structures but remained for the most part unchanged. As the time step reached 200, the film surface predicted by the reduced curvature model reached a stable state and has formed column-like structures throughout the surface. In contrast, the film surface predicted by the current curvature model had just begun to push upward, and it was now at the stage that the reduced curvature model predicted at time step t = 100. The film surface predicted by the current curvature model reached a stable point at the time step about 400. A comparison of the two stable states is shown in Fig. 3.7.

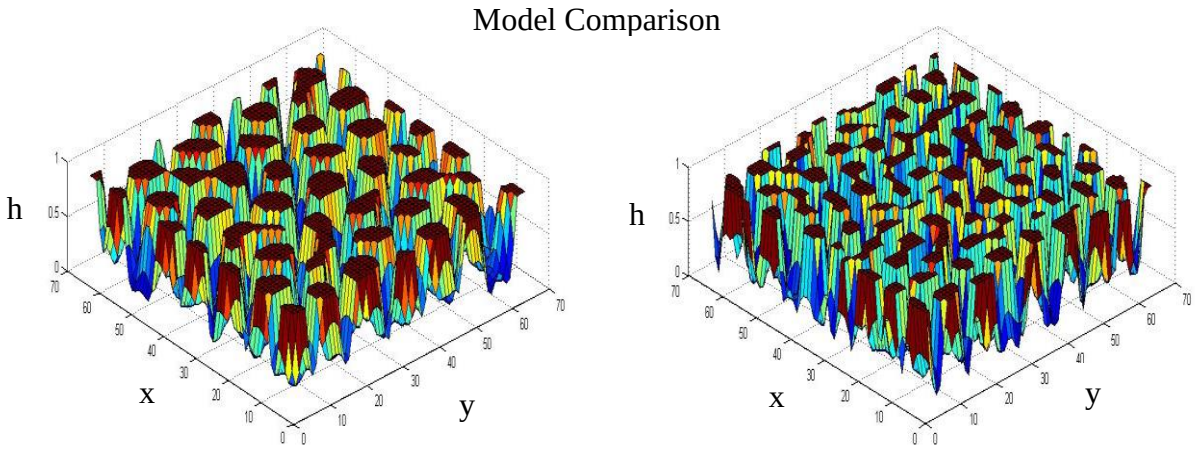

(*a*) Current **(*b*) Reduced**

Figure 3.7: Comparison between the final surface morphologies of the thin films using two different models. (*a*) Current curvature model at *t* = 400, and (*b*) Reduced curvature model at *t* = 200.

Figure 3.7 shows the comparison between the surface morphology of the thin films predicted using the current curvature model [Fig 3.7(*a*)] and the reduced curvature model [Fig 3.8(*b*)]. The spacing between the columns predicted using the reduced curvature model can also be predicted by a linear stability analysis. Considerable such analysis has been performed in the literature and the maximum wavelength is shown to be dependent on the electrostatic forces but

not on the surface tension (Wu et al. 2005). The spacing of columns predicted by the current curvature model deviates from that based on the linear stability analysis is due to elimination of the small-angle approximation. This deviation results in a significant difference of the maximum wavelength or column spacing predicted by the two models. In other words, the current curvature model is capable of predicting more accurate surface morphology of the films during LISA process.

In addition, it is imperative to explore the mass transfer mechanism in order to understand how the patterns form. This study was focused on pressure-driven flow in thin polymer melts and that the competition between the Laplace pressure and the electrostatic pressure dominates the formation of column-shaped structures from the thin films. This does not answer the question of what governs the final distribution of the columns. Comparing the morphologies in Fig. 3.7 clearly shows that changing the surface pressure has an effect on the final shape reached by the polymer, but if that was the case, energetics and control of the polymer properties would be able to design the final shape. It has been speculated that the kinematics of the system has a noticeable effect on the morphology of the surface (Kim & Lu, 2006). This question would need further experimental work to validate. This work was only targeted at formulating an accurate model for simulating the growth of column-shaped structures from polymer films. Understanding of how that growth occurs is fundamental to more accurately guide the polymer into desired surface patterns.

One of the important observations from the simulations is how the material is transported. When looking at the figures, it might be assumed that the columns grow by pushing the material from the bottom of the column to the top, but it is not the case. It is observed in the time steps that the column size remains unchanged until the pillars started to interact with the top electrode,

which causes a sandwiching effect. It is observed that the columns add material to the bottom of the columns from polymer surrounding the bottom of the column, and constantly absorbing new material to the bottom and pushing the column top closer to the top electrode. When a column reaches the top electrode, rich dynamics of the system changes from pulling the film closer to the top electrode to adding material to the bottom of the column. Material is absorbed by each column until there is no polymer left. For this study the average diameter of each column was not measured or recorded, but for other phenomena, the diameters of the created structures are important, such as nanofiber electrospinning, the mass transport mechanism and its effect on the diameter of columns are important.

A unique property of the electrolithography process is the ability to draw patterns in the polymer by controlling the shape of the top electrode. Figure 3.8 demonstrates the patterns predicted by the reduced curvature model and the current model using the same square mask, respectively. It is clear to observe the difference between the two patterns based on different extents of model refinement.

Square Patterned Electrode

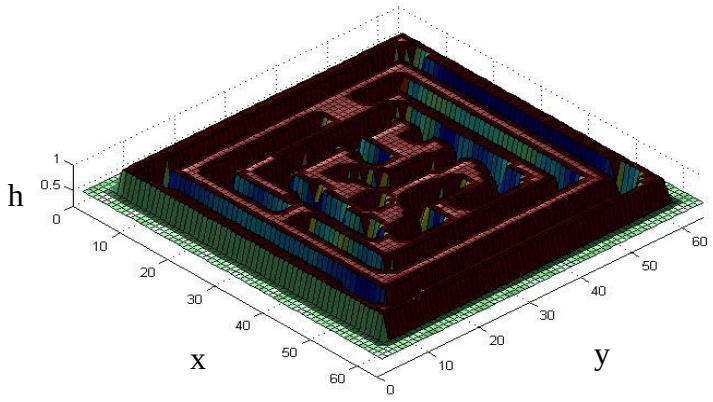

(*a*)

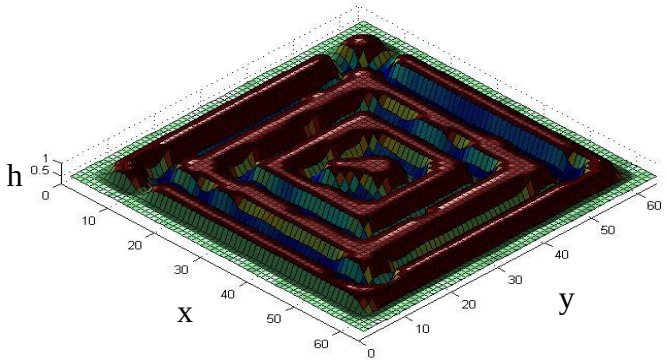

(*b*)

Figure 3.8: Model-predicted square patterns under a square mask: (*a*) Reduced curvature model; and (*b*) Current model. Initial height h_0 = 0.39, dielectric constant ε = 3.5.

Figure 3.9 shows a comparison between the experimental results under a triangle mask and the model-predicted patterns. The model parameters used in the simulation were the initial film height h_0 = 0.39 and dielectric constant of the polymer ε = 3.5.

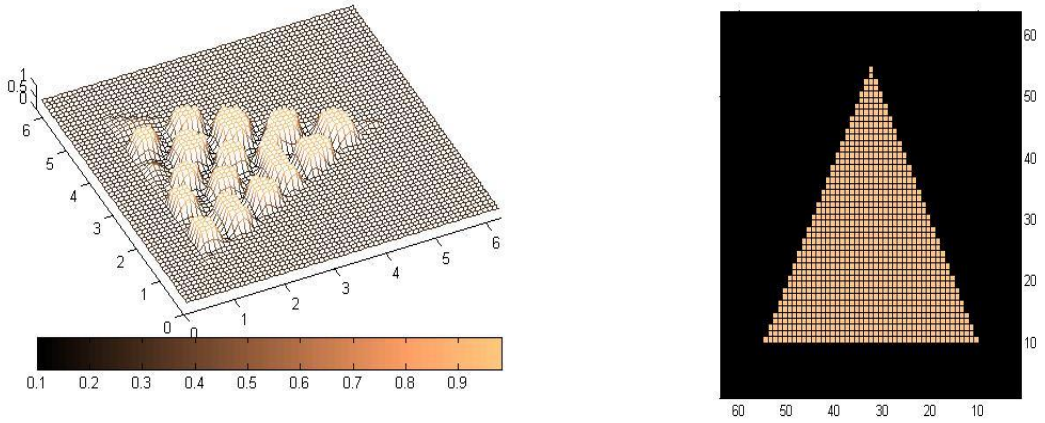

(*a*)

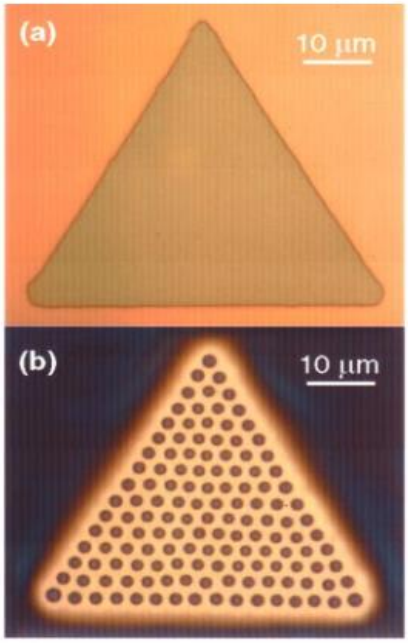

(*a*)

Figure 3.9: Comparison of model-predicted patterns and experimental results. (*a*): Model-predicted pattern and mask; and (*b*): Experimental pattern and mask (Chou & Zhuang, 1999).

To gain a detailed understanding of the model, numerical simulations were run with varying model parameters. The effect of the initial height and different dielectric constants were considered and compared. Figure 3.10 shows the growth of the maximum height for four

different simulations. The initial heights used were h_0 = 0.49, 0.39, 0.29, and 0.19, and dielectric constant was fixed at ε = 3.5.

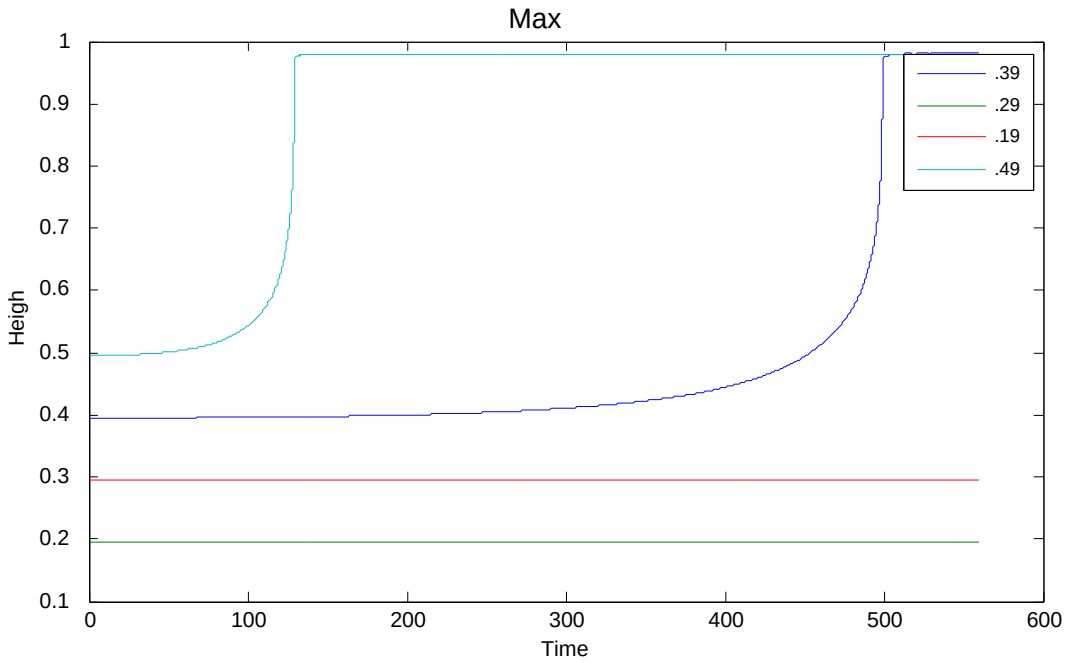

Figure 3.10: Variation of the model-predicted maximum column height with the simulation time for four initial film thicknesses (h_0 = 0.49, 0.39, 0.29, and 0.19).

The diagram shows that the initial film height has an obvious effect on the growth rate of the film. The higher the initial film thickness, the quicker the film surface is going to grow unstable. This can be understood such that a higher electrostatic pressure can be exerted due to the lower gap between the film and the upper electrode for a thicker film.

The dielectric constant shows the similar effect as the initial thickness. Figure 3.11 shows the maximum film height over time for four different values of dielectric constant. The values of dielectric constant used in the simulation were: ε = 4.5, 3.5, 2.5, and 1.5. As the dielectric constant grows, the greater is the growth rate of the film. The increase of growth rate, in this case, is the result of a higher electrostatic pressure caused by a higher dielectric constant.

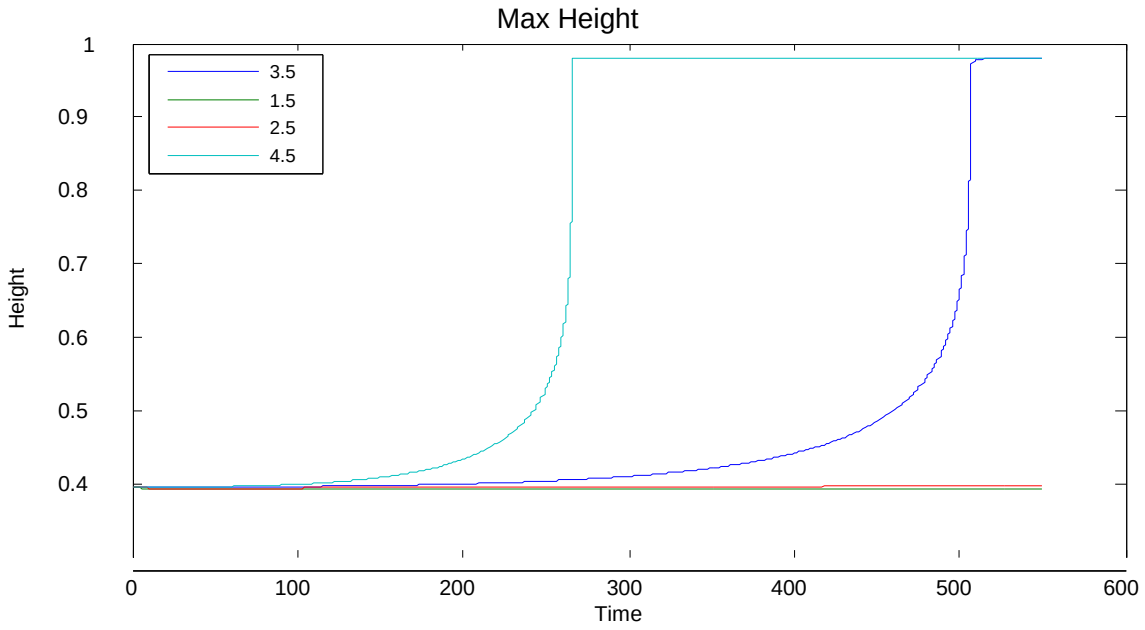

Figure 3.11: Variation of the model-predicted maximum column height with respect to the simulation time for polymer films with four dielectric constants ε = 4.5, 3.5, 2.5, and 1.5, respectively.

Experiments have shown that the instabilities at an air-polymer surface in an electric field will lead to the formation of self-organized columns or structures (Chou et al., 1999; Schaffer et al., 2000; Chou et al., 2001; Lin et al., 2002). The dynamics and nonlinear growth in the formation of the instabilities and late structure formation is the key to understanding such a self-assembly process. This chapter has solved the model developed in Section 3.2 using a finite-difference Fourier-spectral method. The 3D simulations have revealed the unstable, nonlinear growth of thin polymer melts. It has been found that the extent of refinement of the curvature formula used for the Laplace pressure noticeably affected the evolution rate and surface morphology of the thin films. It has also been demonstrated that the film thickness affected the growth rate at which the surface instabilities initiated. By patterning the top electrode, the outside boundary and shape of the emerged pattern can be tuned and optimized. Thus, the study expects the great potential of computer-aided LISA for microelectronics industry in the near future.

The model used in this chapter has provided a great insight into how thin films react under strong electric fields and has given a jumpstart to model the complex process of needleless electrospinning. In needleless electrospinning, the quality of the fiber greatly depends on the shape of the substrate and the viscosity of the solution. In electrolithography, the polymer melt is only a single-phase material that does not contain a solvent. However, in electrospinning process, the effect of the reduced viscosity and drying of the polymer solution due to the solvent evaporation is of great importance to this process. Thus, an electrospinning model capable of accurately capturing the formation of multiple jets from a polymer solution is desired, which can integrate both the electrohydrodynamics of the polymer solution and the varying properties of solution due to the solvent evaporation. In the next chapter, a preliminary needleless electrospinning model will be formulated based on the existing model developed in this chapter, which will take into account the effects of solvent evaporation (drying) and substrate dewetting.

3.5. Summary

In summary, this chapter has formulated a refined LISA model to predict the pattern formation in electrolithography process. The surface morphology evolution predicted in the model closely resembles those available in the literature. The relative simplicity of the refined model allows for an effective, accurate model simulation, which can be conveniently performed on a personal computer. The present model introduced the accurate formula of surface curvature, thus the calculation of the Laplace pressure is exact. The evolution of the film surface is driven by the competition between the Laplace pressure, which stabilizes the surface, and the electrostatic pressure, which destabilizes the surface. The model developed in this chapter can be furthered to capture both the drying and changing viscosity of a two-phase solution, which will be used to study the jet initiation in needleless electrospinning.

4. COMPUTATIONAL SIMULATION OF MULTI-JET INITIATION IN NEEDLELESS ELECTROSPINNING

4.1. Introduction

In Chapter 3, a refined electrohydrodynamic model has been formulated to predict the pattern evolution in thin polymer melts, where only one polymer phase was considered. In this chapter, this refined LISA model developed will be furthered to address the effect of solvent drying in multi-jet initiation in needleless electrospinning process.

The model to be formulated in this chapter is aimed to accurately capture the surface morphology evolution of a dual-component solution. The model will be used to predict how multi-jets initiation from the free surface of a polymer solution as observed in needleless electrospinning. For the purpose of simplicity, the model will continue to adopt the same lubrication theory as adopted in Chapter 3, which does not break the realistic condition in needleless electrospinning process. A robust finite-difference Fourier-spectral method will be formulated for solving a set of two coupled governing PDEs of a drying thin film subjected to an electrostatic field.

The two-component polymer solution is considered for the present modeling, i.e. the polymer solute and a volatile organic solvent. As typically used in needleless electrospinning, the thin layer of the polymer solution is assumed to be incompressible with constant properties across the film thickness. The schematic for this model is shown in Fig. 4.1, similar to that considered in LISA (Fig. 3.1). The top electrode is positioned with a distance H ($H >> h$) above the surface of the thin film. The height of the surface of the polymer solution layer is measured as the distance from the bottom electrode and designated by the variable h.

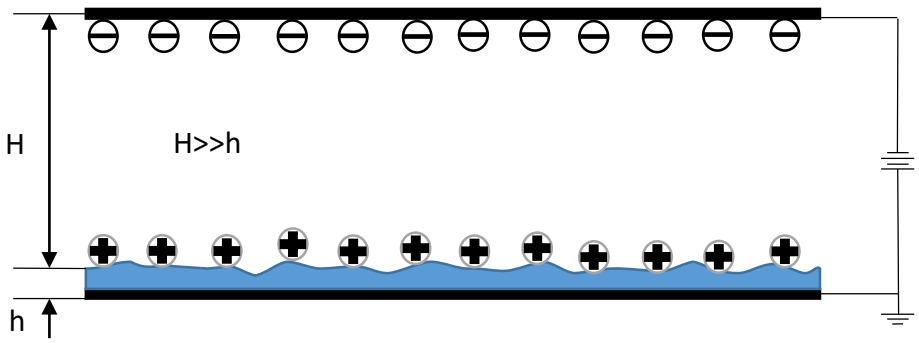

Figure 4.1: Schematic setup of needleless electrospinning.

4.2. Model Formulation

The formulation of this preliminary needleless electrospinning model closely follows the procedure used in Chapter 3. The thickness of the polymer solution layer on the substrate is represented by the variable *h*. To integrate the effect of the solvent evaporation into the evolution of the surface morphology of the thin polymer-solution layer, a simple drying law is added to the kinetic Eq. (3.5) such that

$$\frac{\partial h}{\partial t} = -\nabla \bullet \left(-\frac{h^3}{3\mu} \nabla p \right) - E, \tag{4.1}$$

where E is the evaporation rate with the unit length.time^{-1},

The rate of evaporation has the dimension of speed, which is understood as the thinning rate of the film due to solvent evaporation. The viscosity of the system is represented by μ, which is varying according to a simple exponential law with respect to the solvent volume fraction (Schwartz, 2001). Due to the low thickness of the film, the pressure p and viscosity μ are assumed to be constant across the thin film. The pressure again can be represented by the disjoining pressure p_{dis}, Laplace pressure p_s, and the electrostatic pressure p_e such that

$$p = p_o - p_s - p_e - p_{dis}. \tag{4.2}$$

Herein, the Laplace pressure p_s is approached using the small-slope approximation as used in Eq. (3.13) such that:

$$p_s = \gamma \nabla^2 h, \tag{4.3}$$

where γ is the surface tension, which is assumed to be constant, and $\nabla^2 h$ represents the curvature of the surface. The operator ∇^2 stands for the 2D Laplace operator as $\nabla^2 h = \Delta h = \partial^2 h / \partial x^2 + \partial^2 h / \partial y^2$.

The electrostatic pressure p_e carries the same expression as in Chapter 3. Thus, the electrostatic pressure p_e bears the form

$$p_e = \frac{-U^2 \varepsilon_0 (\varepsilon - 1)\varepsilon}{2[h + (H - h)\varepsilon]^2}, \tag{4.4}$$

where U is the electrostatic voltage, ε is the relative dielectric constant of the solution, ε_0 is the permittivity of free space, and H is the height of the top electrode.

To account for both the effects of dewetting and drying on the surface evolution, the disjoining pressure p_{dis} for this model takes the form (Schwartz, 2001):

$$p_{dis} = \frac{(n-1)(m-1)}{2h_*(n-m)} \gamma \theta_e^2 C \left(\frac{h_*^n}{h^n} - \frac{h_*^m}{h^m} \right), \tag{4.5}$$

where h_* represents the minimum height of the polymer solution layer. The exponents n and m are positive constants with $n > m > 1$. θ_e stands for the static contact angle between the polymer solution and the bottom substrate. The function C accounts for a varying wetting property (e.g., contact angle) of the substrate. For the substrate of uniform wetting properties, C is taken as $C = 1$.

Substitution of Eqs. (4.2)-(4.4) into Eq. (4.1) results in the governing kinetic equation of the evolving film:

$$\frac{\partial h}{\partial t} = -\frac{\gamma}{3\mu}\nabla\bullet\left[h^3\left(\nabla\nabla^3 h + \frac{(n-1)(m-1)}{2h_*(n-m)}\theta_e^2 C\left(\frac{h_*^n}{h^n} - \frac{h_*^m}{h^m}\right) + \frac{-U^2\varepsilon_0(\varepsilon-1)\varepsilon}{2\gamma[h+(H-h)\varepsilon]^2}\right)\right] - E. \quad (4.6)$$

The relatively simple drying law used in this work follows the formulation laid out by Schwartz et al. (2001). The following criteria are stipulated for the drying law to be used in the present formulation.

(a) Solvent is evaporated as the thin film dries;

(b) As the film dries, the viscosity of the layer increases correspondingly;

(c) Thinner film dries more quickly;

(d) The surface evolution is resulted from the competition between the interfacial energetics and drying, which slows and finally stops the motion;

In the present needleless electrospinning model, the thin film is considered to be a mixture of two components, i.e., the non-evaporating polymer solute and the volatile solvent. Such a two-component polymer solution is typically used in electrospinning experiments. Thus, the viscosity of such a two-component solution is a function of the varying volume fraction of the polymer during the drying process. Introduce variable c to stand for the polymer fraction in the solution, which increases as the thin film dries. The composition of the thin layer is treated as uniform across the layer thickness and along the lateral directions before any evaporation takes place. Therefore, the initial polymer fraction is $c = c_0$, where $c_0 < 1$, and is a constant. In addition, variation of the viscosity of the polymer solution with respect to the polymer fraction takes the form such that (Schwartz, 2001)

$$\mu = \mu_o e^{\left[a(c-c_o)\right]}, \quad (4.7)$$

where constant *a* is selected large enough to immobilize the film when the polymer fraction reaches 1 ($c = 1$).

As the polymer fraction *c* approaches one, the rate of evaporation is assumed to decrease to zero. The evaporation function *E* is assumed to take the following form (Schwartz, 2001):

$$E = E_o(1-c)^v, \tag{4.8}$$

where E_0 is the drying rate for a pure solvent and the exponent *v* is in the range:

$$0 \le v < 1. \tag{4.9}$$

Since the solution is considered as a two-component solution, a second evolution equation is needed for tracking the variation of solute (polymer) fraction. The polymer fraction equation needs to be solved simultaneously with Eq. (4.6). When the polymer fraction is treated uniform across the layer thickness, a polymer thickness of the layer can be defined as (Schwartz, 2001):

$$h_P = ch. \tag{4.10}$$

This new thickness leads to the polymer evolution equation as

$$\frac{\partial h_P}{\partial t} = -\nabla\bullet\left[\frac{\gamma c h^3}{3\mu}\left(\nabla\nabla^3 h + \frac{(n-1)(m-1)}{2h_*(n-m)}\theta_e^2 C\left(\frac{h_*^n}{h^n} - \frac{h_*^m}{h^m}\right) + \frac{-U^2\varepsilon_0(\varepsilon-1)\varepsilon}{2\gamma[h+(H-h)\varepsilon]^2}\right)\right]. \tag{4.11}$$

To mitigate the fraction gradient due to quick drying in relatively thin region of the film, a diffusion mixing is added to the polymer evolution. Thus, the full evolution equation of the polymer becomes:

$$\frac{\partial h_P}{\partial t} = -\nabla\bullet\left[\frac{\gamma c h^3}{3\mu}\left(\nabla\nabla^3 h + \frac{(n-1)(m-1)}{2h_*(n-m)}\theta_e^2 C\left(\frac{h_*^n}{h^n} - \frac{h_*^m}{h^m}\right) + \frac{-U^2\varepsilon_0(\varepsilon-1)\varepsilon}{2\gamma[h+(H-h)\varepsilon]^2}\right)\right] + \nabla\bullet(Dh_P\nabla c), \tag{4.12}$$

where *D* is the diffusion constant.

Similar to Chapter 3, non-dimensionalization is evoked herein. The independent parameters, length scale, and time scale that appear in this model are:

$$T=\frac{3\mu_0 h_0^3\gamma}{\left(U^2\varepsilon_0\right)^2},\quad L^2=\frac{\gamma h_0}{\varepsilon_0 U^2},\quad n,\quad m,\quad \tilde{h}=\frac{h}{h_0},\quad \tilde{H}=\frac{H}{h_0}$$

$$\tilde{C}=\frac{f_{nm}\left(1-\cos(\theta_e)\right)\gamma h_0^2}{h_*\varepsilon_0 U^2},\quad f_{nm}=\frac{(n-1)(m-1)}{(n-m)}, \tag{4.13}$$

$$\tilde{E}_o=\frac{TE_0}{h_0},\quad \tilde{D}=\frac{D}{L^2/T},\quad a,\quad c_o,\quad v.$$

Finally, a set of governing kinetic equations of the needleless electrospinning involving electrohydrodynamic multi-jet initiation and drying can be expressed as:

$$\begin{cases}\dfrac{\partial\tilde{h}}{\partial t}=-\nabla\bullet\left[\dfrac{\tilde{h}^3}{e^{a(c-c_0)}}\left(\nabla\nabla^2\tilde{h}+\nabla\left(\tilde{C}\tilde{\Pi}\right)+\dfrac{(\varepsilon-1)\varepsilon}{2[\tilde{h}+(\tilde{H}-\tilde{h})\varepsilon]^2}\right)\right]-\tilde{E}_0\left(1-c\right)^v,\\ \dfrac{\partial\tilde{h}_P}{\partial t}=-\nabla\bullet\left[\dfrac{c\tilde{h}^3}{e^{a(c-c_0)}}\left(\nabla\nabla^2\tilde{h}+\nabla\left(\tilde{C}\tilde{\Pi}\right)+\dfrac{(\varepsilon-1)\varepsilon}{2[\tilde{h}+(\tilde{H}-\tilde{h})\varepsilon]^2}\right)\right]+\nabla\bullet(\tilde{D}\tilde{h}_P\nabla c),\\ h_P=ch.\end{cases} \tag{4.14}$$

The three equations above are to be solved simultaneously for predicting the multi-jet initiation in the early stage of needleless electrospinning process. An efficient finite-difference Fourier-spectral method similar to that in Chapter 3 will be formulated to solve this set of governing equations and track the evolution of surface morphology.

As mentioned in the literature review in Chapter 2, it is possible to predict the maximum wavelength or spacing between pillars via a linear stability analysis (Craster & Matar, 2005; Shankar & Sharma, 2004; Verma et al., 2005; Wu & Chou, 2003; Yang et al., 2013; Li et al., 2014). For multi-jet initiation from a polymer solution, it is also possible to predict the spacing between jets as well. Below shows the simple process to derive the maximum wavelength that emerges from the evolution of the surface morphology of a drying film of polymer solution. The equations are significantly simplified by only considering the stability of a uniform layer of

solution of thickness h_0 with a spatially 1D perturbation. The evaporation of the solvent is also ignored due to destabilization of the thin solution layer is instantaneous. In addition, the entire polymer-solution layer is assumed to be uniform, thus $C = 1$.

To begin, it is assumed that the height of the polymer solution is the initial constant thickness h_0 superimposed with a small random perturbation h_1 $\left(|h_1| << h_0\right)$ such that

$$h = h_0 + h_1 . \tag{4.15}$$

For $h_* << h_0$ and because $n > m$, the disjoining pressure becomes:

$$C\left(\frac{h_*^n}{h^n} - \frac{h_*^m}{h^m}\right) \approx -\frac{h_*^m}{h^m}. \tag{4.16}$$

By defining

$$A = \frac{(n-1)(m-1)\theta_e^2}{2h_*(n-m)}, \tag{4.17}$$

the governing equation of the evolution of the layer height h_1 becomes

$$\frac{\partial h_1}{\partial t} = \frac{-\gamma h_0^3}{3\mu_0}\left[\frac{\partial^4 h_1}{\partial x^4} + \frac{mAh_*^m}{h_0^{m+1}}\frac{\partial^2 h_1}{\partial x^2} + \frac{U^2\varepsilon_o(\varepsilon-1)^2\varepsilon}{\gamma\left[h_o + (H-h_o)\right]^3}\frac{\partial^2 h_1}{\partial x^2}\right]. \tag{4.18}$$

The homogeneous solution to the above PDE is assumed to take the form

$$h_1 = \delta\cos(kx)e^{\omega t}, \tag{4.19}$$

where k is the wave number and ω is the growth rate. Substitution of Eq. (4.19) in Eq. (4.18) leads to the wave dispersion relation, which determines the growth rate dependent on the wave number according to

$$\omega = \frac{-\gamma h_0^3}{3\mu_0}\left[k^4 + \frac{mAh_*^m}{h_0^{m+1}}k^2 + \frac{U^2\varepsilon_o(\varepsilon-1)^2\varepsilon}{\gamma\left[h_o + (H-h_o)\right]^3}k^2\right]. \tag{4.20}$$

The wave number of the maximum growth rate can be found by

$$\frac{\partial \omega}{\partial k} = 0, \tag{4.21}$$

which yields $k_{\max}$ such that

$$k_{\max} = \sqrt{\frac{mAh_*^m}{2h_0^{m+1}} + \frac{U^2 \varepsilon_o \left(\varepsilon - 1\right)^2 \varepsilon}{\gamma \left[h_o + \left(H - h_o\right)\right]^3}}. \tag{4.22}$$

The wavelength corresponding to the maximum growth rate can be determined as

$$\lambda_{\max} = \frac{2\pi}{k_{\max}}. \tag{4.23}$$

4.3. Numerical Scheme

To fully capture the multi-jet initiation at the early state of needleless electrospinning, the efficient, robust finite-difference, Fourier-spectral method is furthered for solving the present set of governing equations. The same notations for inverse and forward Fourier transform are adopted as in Chapter 3.

To begin, the total pressure of the system is calculated. To solve for the Laplace pressure p_s by means of the finite-difference Fourier spectral method, the derivatives are solved in Fourier space via the FFT. Eq. (4.24) shows the process for solving the Laplace pressure equation.

$$p_s = \left(-k^2 \hat{h}\right)_r. \tag{4.24}$$

Once the Laplace pressure p_s is calculated, it can be inputted into the total pressure expression to solve for the pressure.

The pressure equation, Eq. (4.2), can be inputted into the set of evolving equations (4.12) to solve for the updated surface morphology. Thus, Eq. (4.12) can be recast as:

$$\begin{cases} \hat{h}^{n+1} = \hat{h}^{n} - \Delta t\left[ik\bullet\left[\dfrac{(\tilde{h}^{n})^{3}}{e^{a\left(c^{n}-c_{0}\right)}}\left(ikp^{n}\right)_{r} \right]_{k} + \left(\tilde{E}_{0}\left(1-c^{n}\right)^{v} \right)_{k} \right], \\ \hat{h}_{P}^{\ n+1} = \hat{h}_{P}^{n} - \Delta t\left[ik\bullet\left[\dfrac{c^{n}(\tilde{h}^{n})^{3}}{e^{a\left(c^{n}-c_{0}\right)}}\left(ikp^{n}\right)_{r} \right]_{k} - ik\bullet(\tilde{D}\tilde{h}_{P}^{n}\left(ik\hat{c}^{n}\right)_{r})_{k} \right], \\ c^{n+1} = \dfrac{h_{P}^{n+1}}{h^{n+1}}. \end{cases} \tag{4.25}$$

The following flow chart shows the procedure to implement the numerical scheme in Matlab®. The main iterative steps in the flow chart are

- Input all the model parameters and initial conditions.
- Convert the height of the film , h, electrostatic pressure, p_e, and disjoining pressure p_{dis} into Fourier space using the FFT
- Solve for the Laplace pressure p_s using Eq. (4.24).
- Solve for the total pressure of the system and input into Eqs. (4.11) and (4.12)
- Input results into Eq. (4.25)
- Update the surface morphology in physical space by use of the IFFT
- Repeat until the surface morphology reaches the shape that is desired

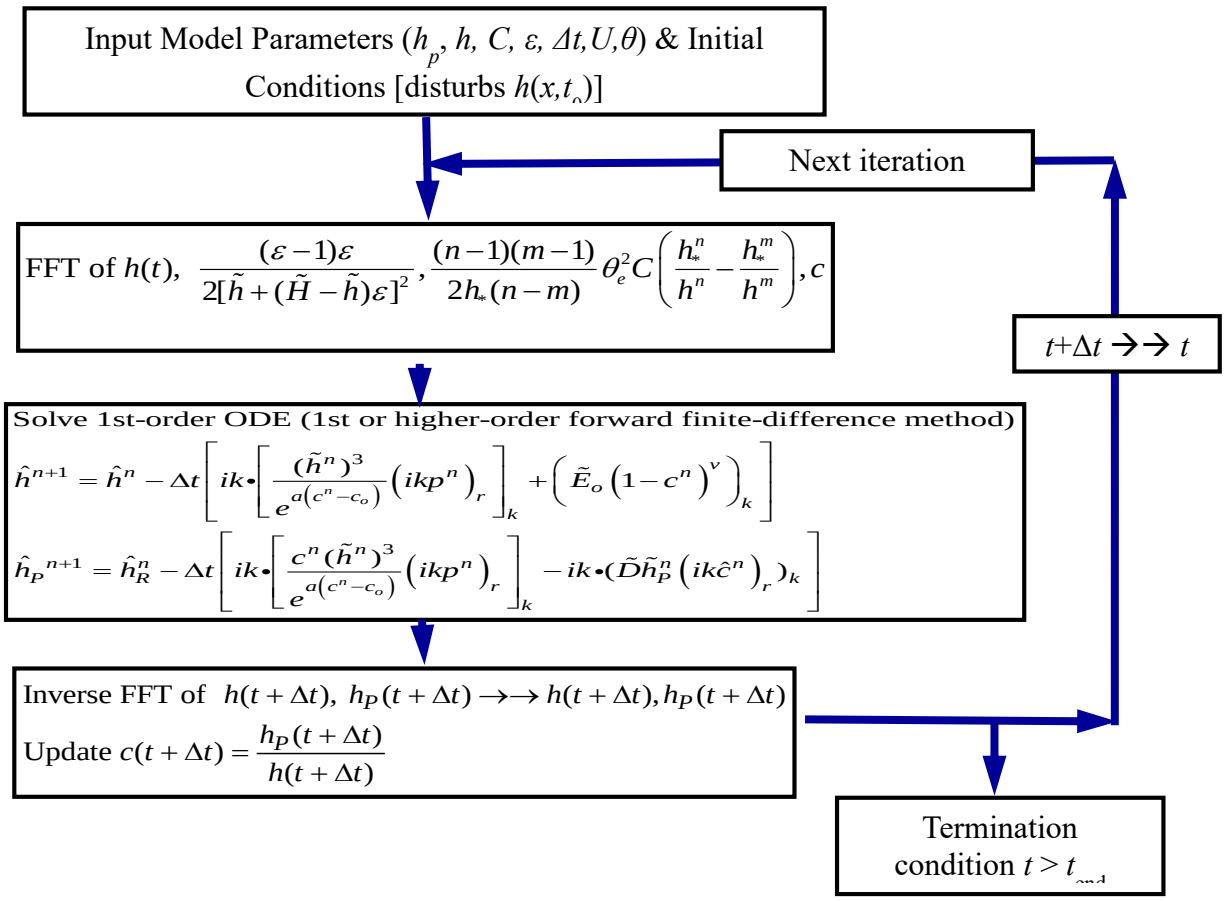

Figure 4.2: Flow chart outlining the numerical iterative procedure for solving the set of governing equations of multi-jet initiation in needleless electrospinning.

4.4. Results

This section presents and discusses the numerical results obtained from a series of numerical simulations based on the model formulated in Section 4.3.

To begin, the model is first validated against thin film flow models without the presence of a strong electric field. The values of the dimensional and nondimensional parameters are tabulated in Table 4.1, which were taken from the literature (Schwartz et al., 2001) and used in the model validation.

Table 4.1:
Parameter Values Used in the Simulations

Physical Quantity	Symbol	Value and Units
Contact angle	θ_e	0.5 rad or 28.7^o
Initial viscosity	μ_o	0.25 p = 0.25 g/(cms)
Surface tension	γ	35 dyn/cm
Initial coating thickness	h_0	50 μm
Disjoining thickness	h_*	5 μm
Evaporation rate	E_0	2 μm/s
Diffusion constant	D	0.1 (dimensionless)
Initial resin fraction	c_0	0.3 (dimensionless)
Viscosity exponent	a	70 (dimensionless)
Evaporation exponent	v	0.5 (dimensionless)

To formulate and validate the present model, the computational work done by Schwartz et al. (2001) played a significant role. Schwartz et al. (2001) developed a model for the reticulation of surface coatings of resins dissolved in volatile organic solvents, in which regular finite difference method was utilized for both temporal and spatial integration. The effect of substrate defects on the reticulation is modeled and validated by experimental results (Schwartz et al., 2001). Schwartz's model was the inspiration for the refined electrohydrodynamic model in the present study.

The below numerical results show the effect of substrate defects on thin film evolution. For each defect site, the contact angle was taken to be about 15% larger than its surrounding substrate. It is assumed that the initial height was uniform with tiny random perturbation and had a uniform polymer fraction. Figure 4.3 shows the defect pattern used in the simulation and the evolution of the thin film over a few dimensionless time steps from the literature. Results from the current model are shown in Fig. 4.4.

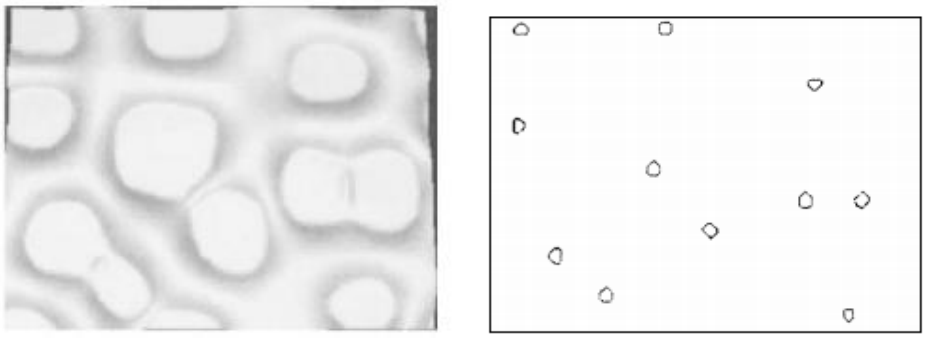

(*A*) **(*B*)**

Figure 4.3: (*A*) Thin Film morphology after 1.3 seconds; and (*B*) Defect pattern used to initiate the film evolution. (Schwartz, 2001).

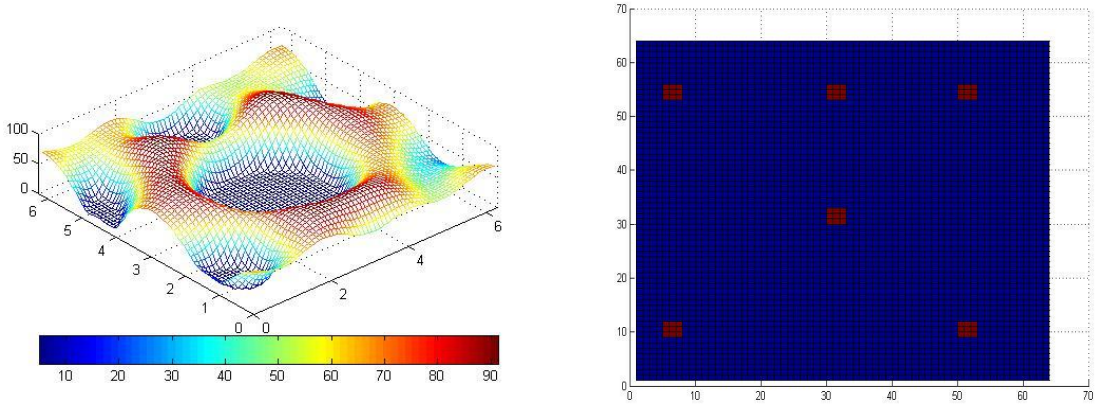

(*A*) **(*B*)**

Figure 4.4: (*A*) Thin Film morphology after 1.5 seconds; and (*B*) Defect pattern used to initiate the film evolution.

Figure 4.3 from the literature and Fig. 4.4 from the current model show the similar morphologies; therein the regions with the contact angle 15% larger dewet faster than the surrounding substrate. The higher contact angle caused the perturbation and drove the thin film to evolve. These similarities indicate that the current model is able to track the thin film evolution. The next step is to track the thin film evolution in an electric field, which is also the multi-jet intiation at the early state of needleless electrospinning.

The numerical results were obtained based on the parameters and characteristic units formulated in the previous section. The electric field is expected to have significant effect on the surface morphology. The values of the dimensional and nondimensional parameters are tabulated in Table 4.2 and employed in the present computational simulations (Schwartz et al., 2001). For each simulation case, the computational cell consisted of a mesh with size 64 × 64. By examing the results using finer or coarser meshes, the influence of gride size on the computed results was not significant due to employing the high-accuracy Fourier spectral method.

Table 4.2:
Parameter Values Used in the Simulations

Physical Quantity	Symbol	Value and Units
Contact angle	θ_e	0.5 rad or 28.7^o
Initial viscosity	μ_0	0.25 p = 0.25 g/(cms)
Surface tension	γ	35 dyn/cm
Initial coating thickness	h_0	50 μm
Disjoining thickness	h_*	5 μm
Evaporation rate	E_o	2 μm/s
Diffusion constant	D	0.1 (dimensionless)
Initial resin fraction	c_0	0.3 (dimensionless)
Viscosity exponent	A	70 (dimensionless)
Evaporation exponent	V	0.5 (dimensionless)
Voltage	U	50,000 Volts
Permittivity of free Space	ε_0	8.85 x 10^{-12}
Dielectric constant	ε	45
Max height	H	5 cm

To compare how the electric field affects the evolution of the thin polymer solution, several simulations were carried out with varying model parameters. Figure 4.5 shows the surface morphology using the same defect pattern as Fig. 4.4. Figure 4.6 shows the surface morphology based on a line grid defect.

Dot

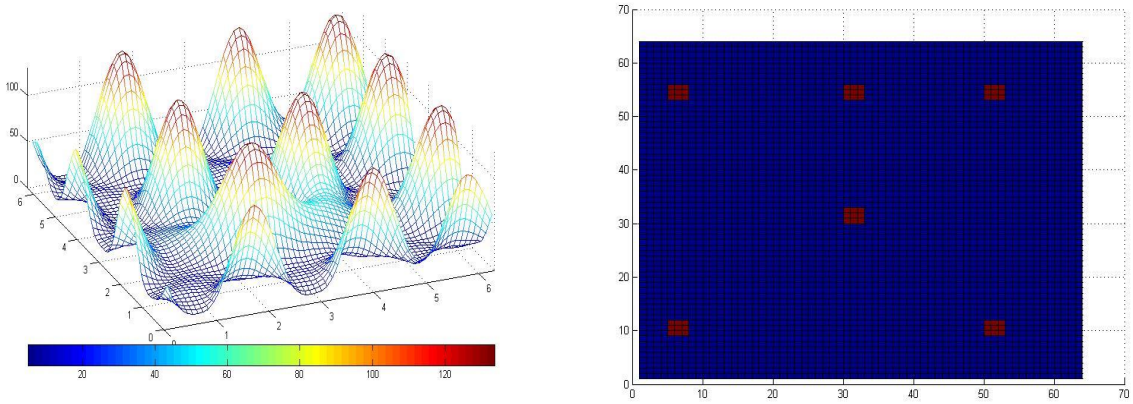

(*A*) **(*B*)**

Figure 4.5: (*A*) Surface morphology after 1.0 second in an electric field; (*B*) Defect pattern used to drive surface evolution.

Line

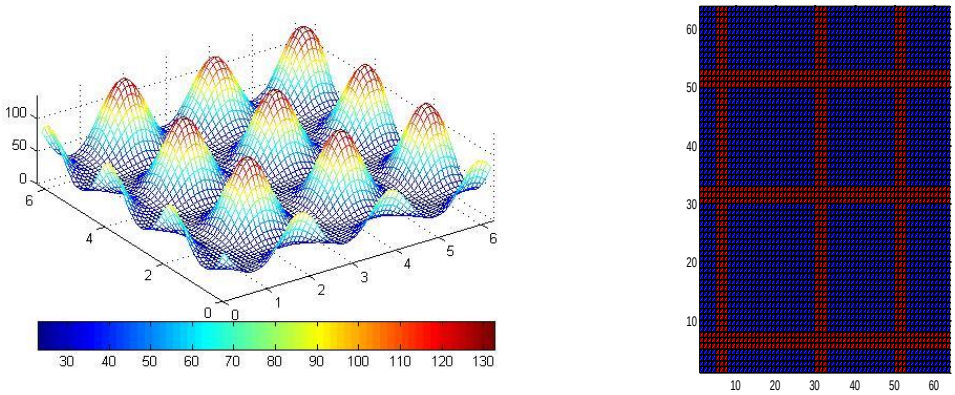

(*A*) **(*B*)**

Figure 4.6: (*A*) Surface morphology after 1.0 second in an electric field; and (*B*) Defect pattern used to drive surface evolution.

As interpreted in the literature review, the surface evolution in the needleless electrospinning process is assumed to follow the process: a thin layer of polymer solution is covered on the surface spinneret, small perturbation on the film causes the film to form into multiple cone-shaped spikes; when the electric forces reach a critical value, cone-shaped

structures form into “Taylor cones”; finally, the jets are stretched out from the “Taylor cones”, resulting into multiple fibers. As observed in Fig. 4.3, multiple cone-shaped spikes have formed only after one second. Due to the relative simplicity of this model, the present model could not be used to determine the next stage in the evolution process due to the model breaking the no-penetration condition of the bottom substrate.

Even though the model is relatively simple, the above results shown in Fig. 4.4 do not diminish the effect of electric field on the evolution of thin polymer solutions. Also, it has been determined that the drying does not have a significant effect on the final morphology of the solution since substrate dewetting has an instantaneous effect. Since drying does not have an effect on the surface morphology in the present study, it is determined that it is the perturbation caused by the defects on the surface and the electric field, which drive the surface evolution and multi-jet initiation. The difference of the surface morphologies between Figs. 4.5 and 4.6 validates this phenomenon. Also as shown in Fig. 4.7, the patterns were formed at the immediate moments after the start of the evolution since dewetting phenomenon has its instantaneous effect. The figure shows both the initial moments for the line defects as well as the circle defects.

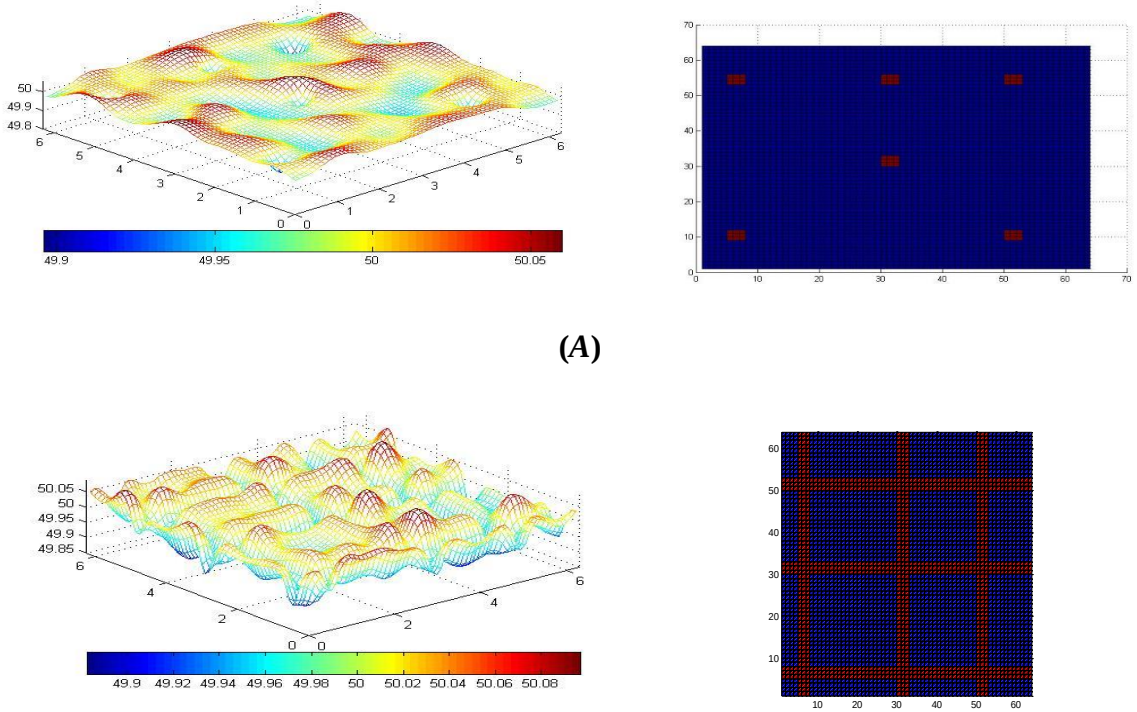

Figure 4.7: Initial stages of surface evolution driven by defect patterns in needleless electrospinning. (*A*): Circle defect pattern; (*B*) Line defect pattern.

As the evolution starts, the solution builds up around the edges of the defect, which allows for the electrostatic force to easily drive the surface destabilization. Once the surface grows unstable, the cone-shaped structures start to grow from the solution to form multi-jets at the later stage. This further proves that it is the defects of substrate and the electric field that drive the initial stages of multi-jet initiation in needleless electrospinning process. This is further proven by Figs. 4.8 and 4.9, which show that the surface property of the substrate has a significant effect on the growth rate of the thin liquid film. The line defects reach the maximum height far quicker than the dotted defects. This observation is held because more substrate is at a higher contact energy causing significantly large perturbation at the initial stage of evolution.

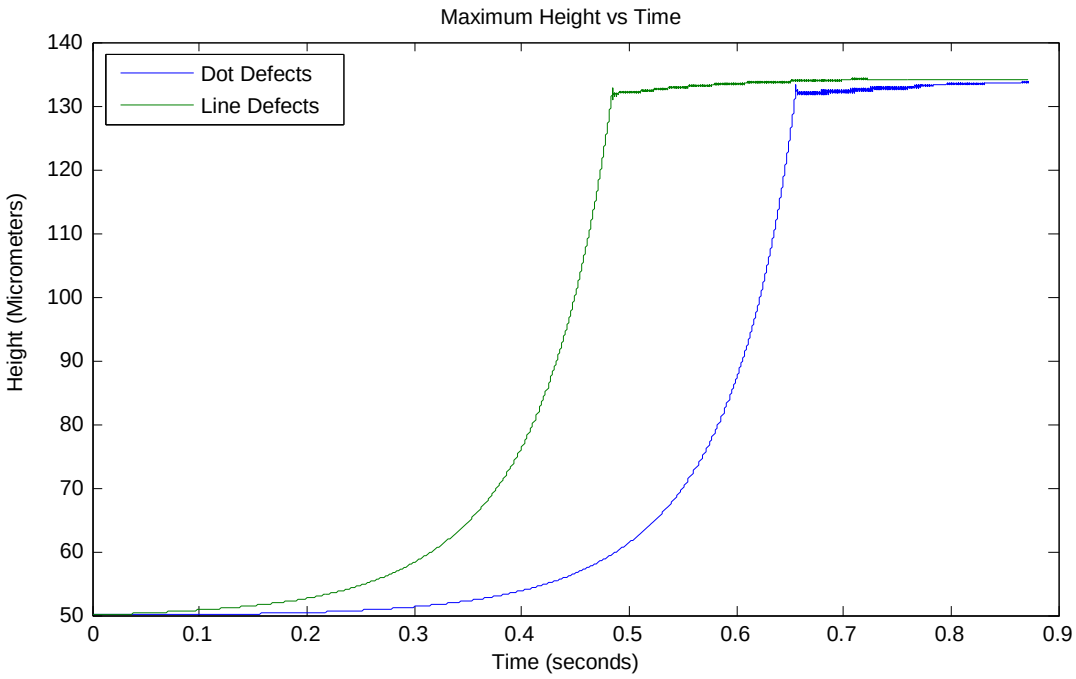

Figure 4.8: Comparison of the maximum height growth over time between the two defect types.

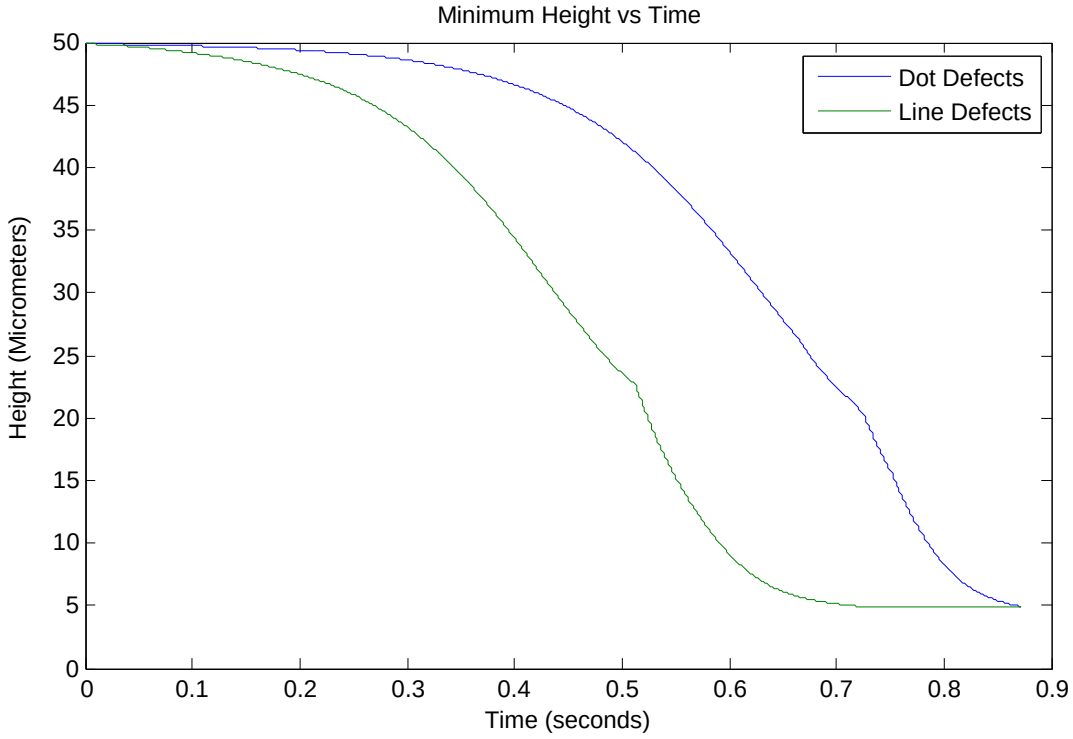

Figure 4.9: Comparison of the minimum height growth over time between the two defect types.

To capture the effects of the model parameters on the simulation, a comparative study was performed to examine each model parameter. The first model parameter under consideration was the effect of the initial polymer fraction on the final surface morphology. Each simulation had the initial height h_0 = 50 μm, voltage U = 50 kV, and dielectric constant ε = 45. Three different values of the initial polymer fraction were compared, i.e., c_0 = 0.3, 0.6, and 0.9, Fig. 4.10 shows the three model-predicted surface morphologies. It can be found from the three simulations that the initial polymer volume fraction does not have a profound effect on the initial stages of needleless electrospinning. This would also show that the model viscosity of the system does not have an effect on the initial stages of needleless electrospinning as well. It has been shown that for traditional needle-based electrospinning, the polymer fraction has a great effect on the fiber diameter (Shenoy et al., 2005; Niu et al., 2009). The difference could be from the needle limits size and shape of the "Taylor cone" generated from the tip. With a free surface of the polymer solution, the "Taylor cone" is allowed to generate more naturally thus allowing for more natural mass transportation. With more natural mass transport, the amount of polymer would not affect the formation of the "Taylor cone". It is obvious that the current model needs to be further refined significantly in order to fully model the entire needleless electrospinning process from the initial flat film to fiber generation from a "Taylor cone".

Initial Polymer Concentration

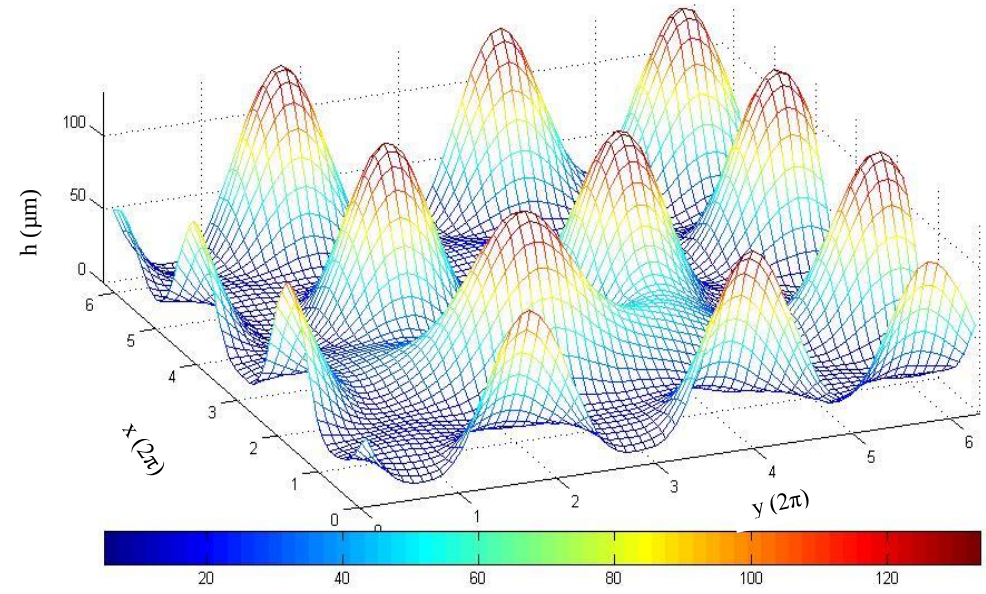

(*A*)

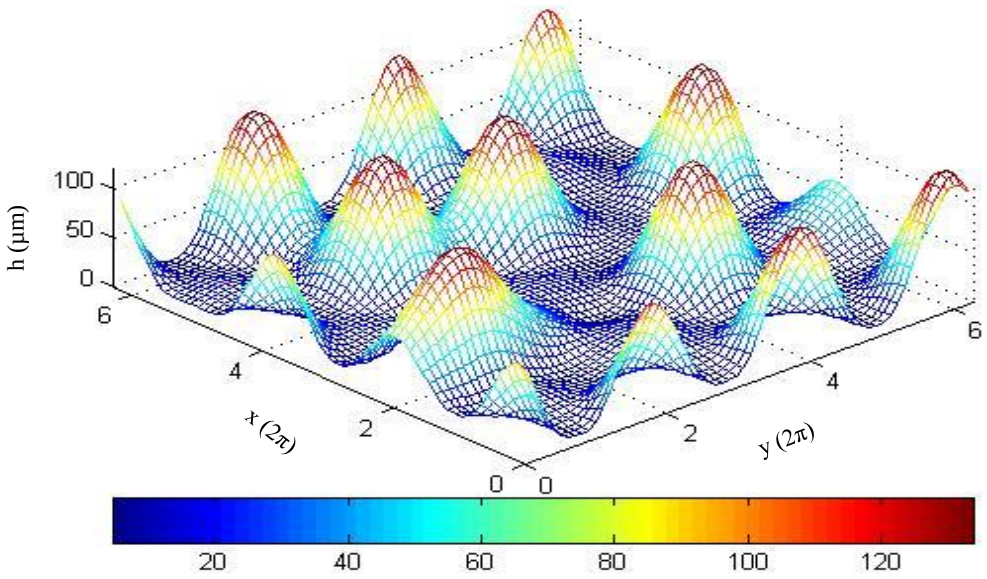

(*B*)

Figure 4.10: Comparison of the final morphologies for varying initial polymer fractions. (*A*) c_0 = 0.3; (*B*) c_0 = 0.6; and (*C*) c_0 = 0.9.

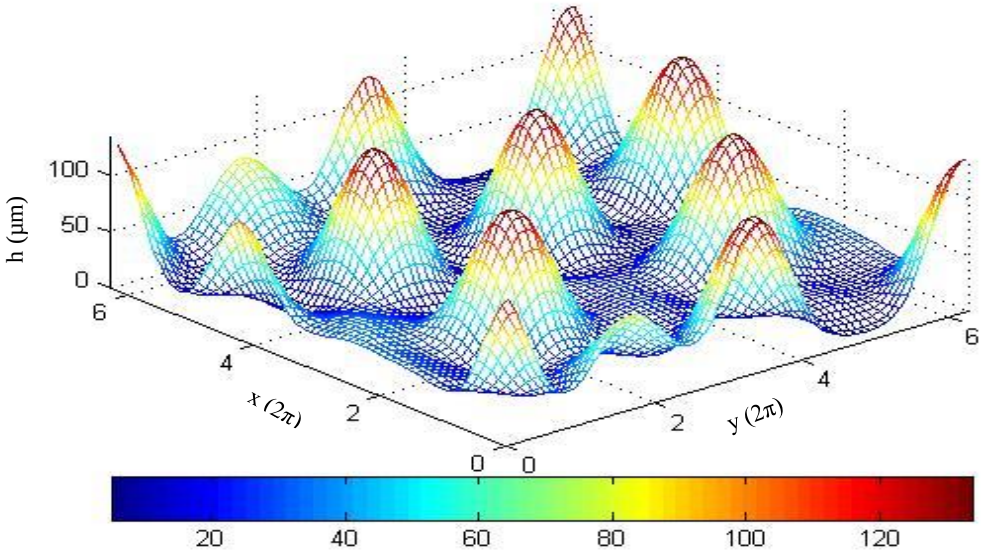

(*C*)

Figure 4.10: Comparison of the final morphologies for varying initial polymer fractions (continued). (*A*) c_0 = 0.3; (*B*) c_0 = 0.6; and (*C*) c_0 = 0.9.

The next model parameter under consideration was the dielectric constant ε. It has been shown that for needle-based electrospinning, the dielectric constant has a significant effect on the fiber diameter. Luo et al. (2012) showed that fiber diameters less than 100 nm were achieved when the dielectric constant was above 19. Below 19 the fibers produced had diameters from sub-micrometer to millimeter (Luo et al., 2012). Other initial conditions under consideration were those displayed in Table 4.2. Three values of dielectric constant ε = 25, 35, and 45 were used for the simulation. Figure 4.11 shows the three results from the simulations.

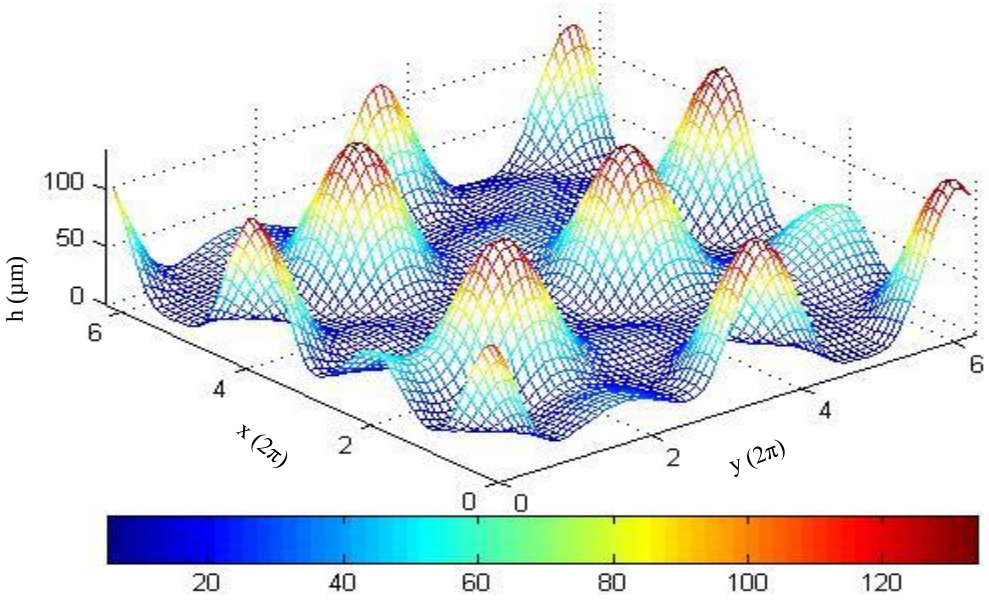

(*A*)

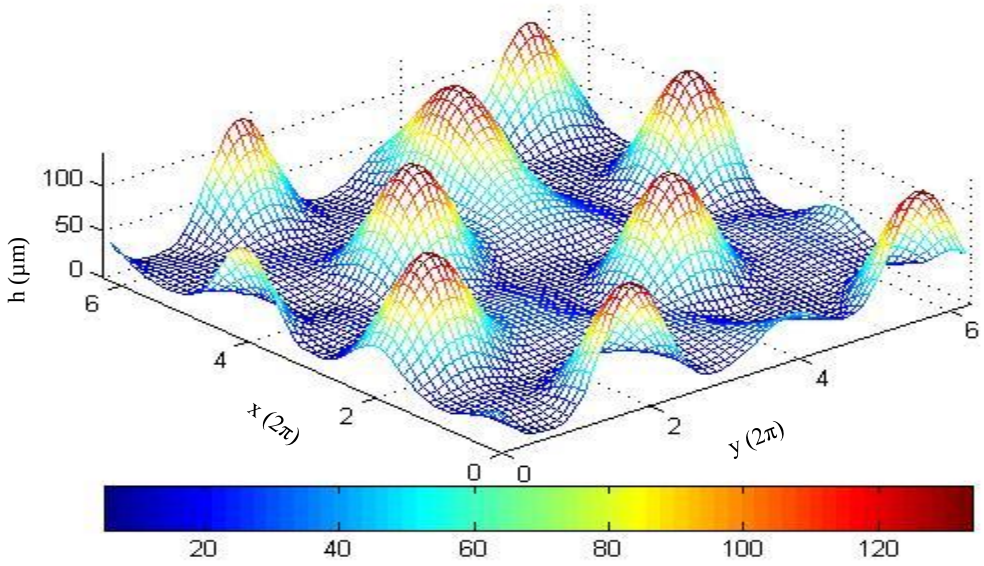

(*B*)

Figure 4.11: Comparison of the effect of dielectric constant on the final surface morphology: (*A*) ε = 25; (*B*) ε = 35; (*C*) ε = 45.

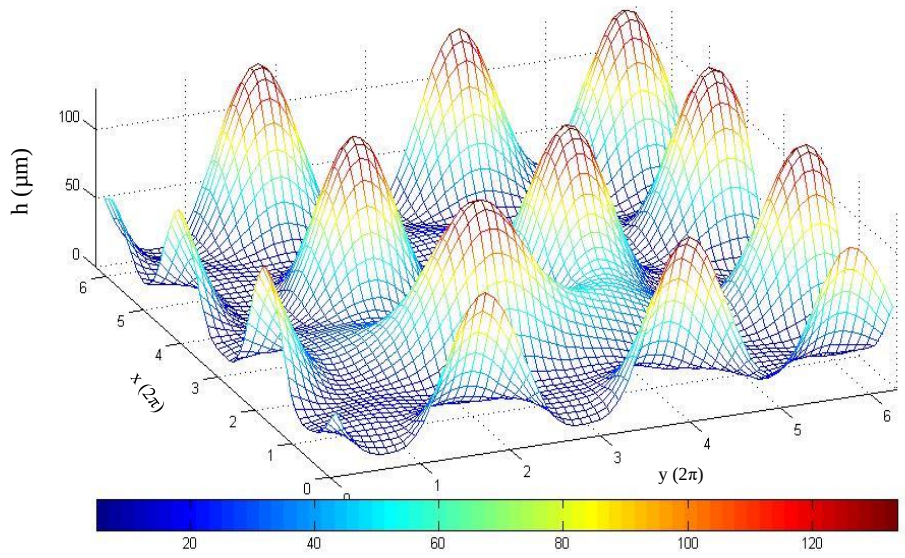

(*C*)

Figure 4.11: Comparison of the effect of dielectric constant on the final surface morphology: (*A*) ε = 25; (*B*) ε = 35; (*C*) ε = 45 (continued).

The above results show that the dielectric constant has no significant effect on the initial morphology evolution, but shows noticeable effect on the spacing and number of features of the morphology. It can be understood that at the lower dielectric constant values, the solution is not strongly affected by the electric field. Figure 4.12 shows the growth of the maximum height over time. It is shown that the dielectric constant does not seem to cause the film to grow faster at higher levels, even that the dielectric constant does not have any effect on the rate of growth. In addition, Eqs. (4.22) and (4.23) predict that at higher dielectric constants, the spacing between features would be smaller.

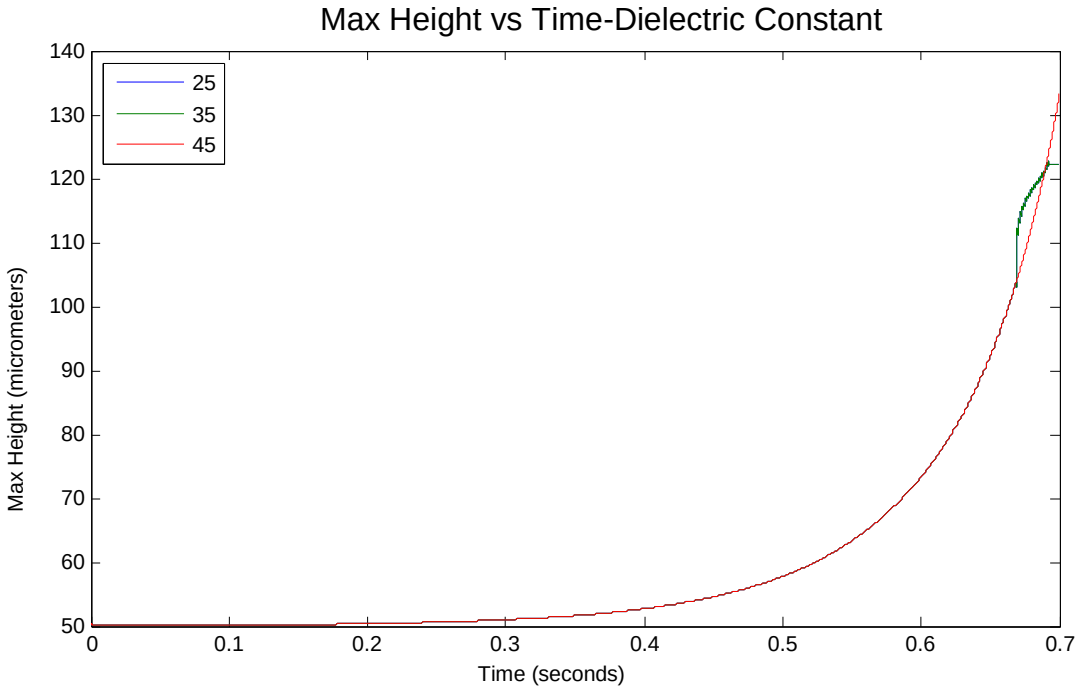

Figure 4.12: Comparison of the growth of the maximum height for three different dielectric constants: ε = 25, 35, and 45.

The next model parameter under consideration was the electric voltage. Three voltages were used for this study: U = 50 kV, 75 kV, and 100 kV. These voltages are in line with what were used in experimental studies of needleless electrospinning (Nui et al., 2009; Wang et al., 2012; Jirsak et al., 2009). Figure 4.13 shows the numerical results of the surface morphology when the drying film is subjected to three different voltages above, respectively.

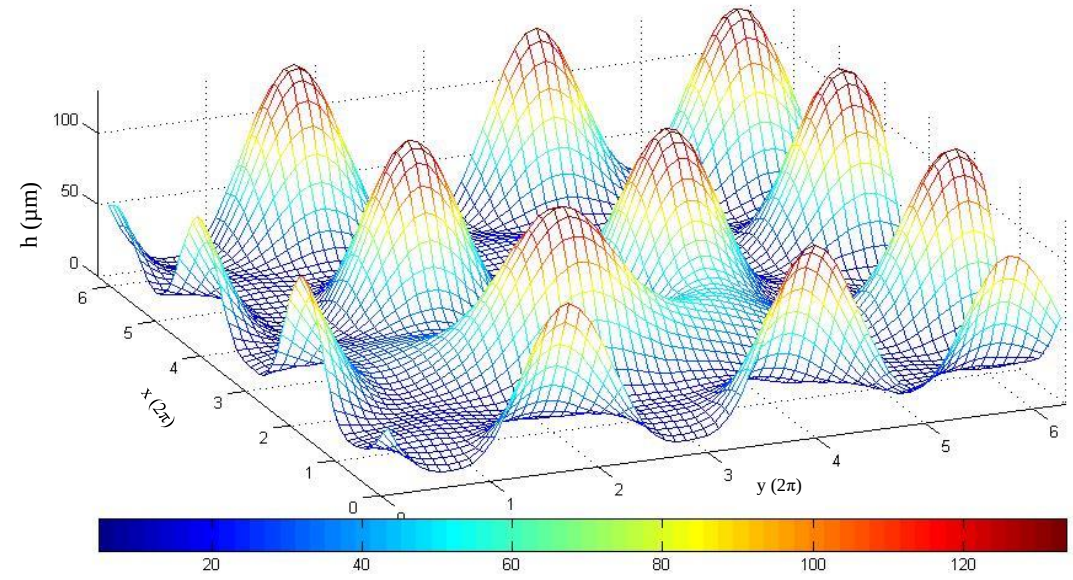

(*A*)

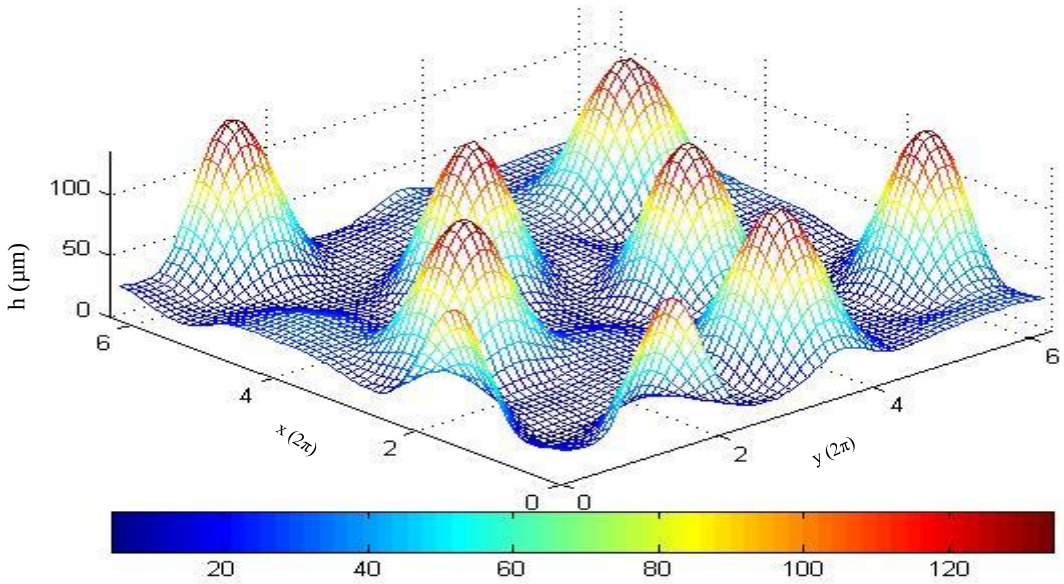

(*B*)

Figure 4.13: Effect of the applied voltage on the initial evolution of the surface morphology. (*A*): *U* = 50 kV; (*B*): *U* = 75 kV; (*C*): *U* = 100 kV.

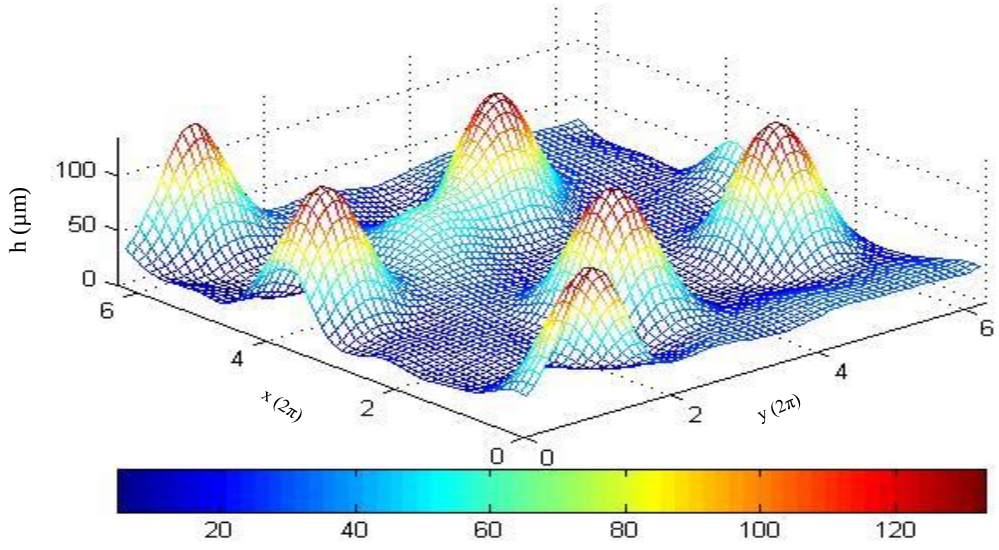

(*C*)

Figure 4.13: Effect of the applied voltage on the initial evolution of the surface morphology (continued). (*A*): *U* = 50 kV; (*B*): *U* = 75 kV; (*C*): *U* = 100 kV.

In Fig. 4.13, it is found that the applied voltage of the system seems to have a significant effect on the surface morphology. As the voltage increases, less cones are formed on the surface over the same amount of time. This implies a counter-intuitive result such that with a higher voltage, the electric field is expected to enhance the surface destabilization; however, according to Eqs. (4.22) and (4.23), the higher the voltage the closer together the features should be to each other.

4.5. Summary

In conclusion, the model formulated in this chapter has been used to simulate the initial stages of needleless electrospinning. The model was able to efficiently handle the dual-component solution used in the simulations. The effect of model parameters (e.g., defect pattern on the substrate, dielectric constant, applied voltage, etc.) on the initial stages of needleless electrospinning was examined. By comparing the surface morphologies based on the

computational results, it was found that substrate defects have a dominating effect on the evolution of surface morphology. Due to the limitation of lubrication theory, 3D multi-physics model is still desired in order to capture the entire process of needleless electrospinning.

5. SUMMARY AND FUTURE RESEARCH

Recently developed needleless electrospinning and electro-lithography are two successful nanofabrication techniques that have been utilized extensively for low-cost, scalable, and continuous fabrication of nanofibers and patterned thin films. Rational understanding of the fundamental electrohydrodynamic principles underneath these nano-manufacturing methods is crucial to controllable fabrication of these nanomaterials. This research project was aimed to formulate robust, high-efficiency finite-difference Fourier spectral methods for numerical simulation of the electrohydrodynamic evolution of thin polymer films, particularly the surface destabilization under electrostatic field. Two electrohydrodynamic thin-film models have been considered and refined. The first was based on reduced lubrication theory; the second further took into account the effect of solvent drying and dewetting of the substrate. FFT based spectral method was integrated into the finite difference algorithms for fast, accurately solving the resulting governing nonlinear PDEs of the evolving systems. The present methods have been used to examine the dependencies of the evolving surface features of the thin films upon the model parameters, e.g., the dielectric constant, film thickness, mask shape and thickness, etc. The numerical results predicted by the present simulations were validated by those available in the literature. The present study can be used for fast, controllable nanofabrication.

Specifically, Chapter 3 has formulated a refined LISA model to predict the pattern formation in the electrolithography process. The surface morphology evolution predicted in the model closely resembles those available in the literature. The relative simplicity of the refined model allows for an effective, accurate model simulation, which can be conveniently performed on a PC. The present model introduced the accurate formula of surface curvature, thus the calculation of the Laplace pressure is exact. The evolution of the film surface is driven by the

competition between the Laplace pressure, which stabilizes the surface, and the electrostatic pressure, which destabilizes the surface. The model developed in Chapter 3 can be furthered to capture both the drying and changing viscosity of a two-phase solution, which will be used to study the jet initiation in needleless electrospinning.

In Chapter 4, a new model was formulated to simulate the initial stages of needleless electrospinning involving solvent evaporation and surface dewetting. The model was able to efficiently handle the dual-component solution used in the simulations. The effect of model parameters (e.g., defect pattern on the substrate, dielectric constant, applied voltage, etc.) on the initial stages of needleless electrospinning was examined. By comparing the surface morphologies based on the computational results, it was found that substrate defects have a dominating effect on the evolution of surface morphology. Due to the limitation of lubrication theory, 3D multi-physics model is still desired in order to capture the entire process of needleless electrospinning.

The models developed in this thesis show a strong potential in predicting the evolution of thin films. However, the relative simplicity of the models limits the full measure of the physical phenomenon taking place. To handle the more complex physical phenomenon. a fully 3D model would have to be developed. A fully 3D model would be able to capture much more complicated phenomenon including nonuniform drying or material parameters, as well as removing the assumption of the lubrication theory. This would allow for a more realistic approach in modeling the surface evolution in needleless electrospinning process.

In conclusion:

- Chapter 3 developed a model to predict the formation of periodic pillar arrangements from thin polymer melts.

- The curvature formula was refined to exactly calculate the Laplace pressure of the system
- Chapter 4 further enhanced the model formulated in Chapter 3 by taking into account a two-phase solution to rationally understand the formation of multiple jets in needleless electrospinning.
- Variable viscosity and drying of the thin film were added to account for a volatile solvent.
- It was shown that the substrate defects dominate the initial seconds of surface morphology evolution in needleless electrospinning.
- The relative simplicity of the model does not allow for more complex drying and material parameters.
- Fully 3D models still need to be developed that can handle the complex drying and evolution of a thin layer of polymer solution as well as the complex dynamics seen in the formation of solid fibers from a liquid jet in needleless electrospinning.

REFERENCES

Bognitzki, M., Frese, T., Steinhart, M., Greiner, A., Wendorff, J. H., Schaper, A., & Hellwig, M. (2001). Preparation of fibers with nanoscaled morphologies: electrospinning of polymer blends. *Polymer Engineering and Science*, *41*(6), 982-989.

Cengiz, F., Dao, T. A., & Jirsak, O. (2010). Influence of solution properties on the roller electrospinning of poly (vinyl alcohol). *Polymer Engineering & Science, 50*(5), 936-943.

Chou, S. Y., Zhuang, L., & Guo, L. (1999). Lithographically induced self-construction of polymer microstructures for resistless patterning. *Applied Physics Letters*, *75*(7), 1004-1006.

Chou, S. Y. (2001). Nanoimprint lithography and lithographically induced self-assembly. *MRS Bulletin*, *26*(07), 512-517.

Craster, R., & Matar, O. (2005). Electrically induced pattern formation in thin leaky dielectric films. *Physics of Fluids , 17*(3), 032104.

Dzenis, Y. (2004). Spinning continuous fibers for nanotechnology. Science 304, 1917–1919.

Fong, H., Chun, I., & Reneker, D. H. (1999). Beaded nanofibers formed during electrospinning. *Polymer*, *40*(16), 4585-4592.

Gottlieb, D., Orszag, S. A., & MA, C. H. I. (1977). *Numerical Analysis of Spectral Methods*: SIAM.

Greiner, A., & Wendorff, J. H. (2007). Electrospinning: a fascinating method for the preparation of ultrathin fibers. *Angewandte Chemie International Edition, 46*(30), 5670-5703.

Jirsak, O., Sanetrnik, F., Lukas, D., Kotek, V., Martinova, L., & Chaloupek, J. (2009). Method of nanofibres production from a polymer solution using electrostatic spinning and a device for carrying out the method: Google Patents.

Kim, D., & Lu, W. (2006). Three-dimensional model of electrostatically induced pattern formation in thin polymer films. *Physical Review B, 73*(3), 035206.

Li, D., & Xia, Y. (2004). Electrospinning of nanofibers: reinventing the wheel? *Advanced Materials, 16*(14), 1151-1170.

Li, H., Yu, W., Wang, Y., Bu, H., Liu, Z., Abraham, E., & Desmulliez, M. (2014). Simulation of the electrohydrodynamic instability process used in the fabrication of hierarchic and hollow micro/nanostructures. *RSC Advances, 4*(27), 13774-13781.

Li, H., Yu, W., Zhang, L., Liu, Z., Brown, K., Abraham, E., . . . Bailey, C. (2013). Simulation and modelling of sub-30 nm polymeric channels fabricated by electrostatic induced lithography. *RSC Advances, 3*(29), 11839-11845.

Li, Z., & Wang, C. (2013). Effects of working parameters on electrospinning *One-Dimensional Nanostructures* (pp. 15-28): Springer.

Lin, Z., Kerle, T., Russell, T. P., Schäffer, E., & Steiner, U. (2002). Structure formation at the interface of liquid/liquid bilayer in electric field.*Macromolecules*, *35*(10), 3971-3976.

Luo, C. J., Stride, E., & Edirisinghe, M. (2012). Mapping the influence of solubility and dielectric constant on electrospinning polycaprolactone solutions.*Macromolecules*, *45*(11), 4669-4680.

Niu, H., Lin, T., & Wang, X. (2009). Needleless electrospinning. I. A comparison of cylinder and disk nozzles. *Journal of Applied Polymer Science*, *114*(6), 3524-3530.

Pease, L. F., & Russel, W. B. (2002). Linear stability analysis of thin leaky dielectric films subjected to electric fields. *Journal of Non-Newtonian Fluid Mechanics, 102*(2), 233-250.

Reneker, D. H., & Chun, I. (1996). Nanometre diameter fibres of polymer, produced by electrospinning. *Nanotechnology*, *7*(3), 216.

Reneker, D. H., Yarin, A. L., Zussman, E., & Xu, H. (2007). Electrospinning of nanofibers from polymer solutions and melts. *Advances in Applied Mechanics*,*41*, 43-346.

Schäffer, E., Thurn-Albrecht, T., Russell, T. P., & Steiner, U. (2000). Electrically induced structure formation and pattern transfer. *Nature*, *403*(6772), 874-877.

Schwartz, L. W., Roy, R. V., Eley, R. R., & Petrash, S. (2001). Dewetting patterns in a drying liquid film. *Journal of Colloid and Interface Science, 234*(2), 363-374.

Shankar, V., & Sharma, A. (2004). Instability of the interface between thin fluid films subjected to electric fields. *Journal of Colloid and Interface Science, 274*(1), 294-308.

Simm, W., Gosling, C., Bonart, R., & Falkai, B. V. (1979). Fibre fleece of electrostatically spun fibres and methods of making same: Google Patents.

Taylor, G. I. (1969). Electrically driven jets. Proceeding of the Royal Society of London: Mathematic and Physical Sciences A313, 453–475.

Verma, R., Sharma, A., Kargupta, K., & Bhaumik, J. (2005). Electric field induced instability and pattern formation in thin liquid films. *Langmuir, 21*(8), 3710-3721.

Wang, Q., Tahir, M., Zang, J., & Zhao, X. (2012). Dynamic electrostatic Lithography: Multiscale on-demand patterning on large-area curved surfaces. *Advanced Materials, 24*(15), 1947-1951.

Wang, X., Niu, H., Wang, X., & Lin, T. (2012). Needleless electrospinning of uniform nanofibers using spiral coil spinnerets. *Journal of Nanomaterials, 2012*, 3.

Wu, N., Pease, L. F., & Russel, W. B. (2005). Electric-field-induced patterns in thin polymer films: Weakly nonlinear and fully nonlinear evolution. *Langmuir, 21*(26), 12290-12302. doi: 10.1021/la052099z

Wu, L., & Chou, S. Y. (2003). Dynamic modeling and scaling of nanostructure formation in the lithographically induced self-assembly and self-construction. *Applied Physics Letters, 82*(19), 3200-3202.

Wu, X.-F., & Dzenis, Y. A. (2005). Electrohydrodynamic instability of thin conductive liquid films. *Journal of Physics D: Applied Physics, 38*(16), 2848.

Yang, Q., Li, B. Q., & Ding, Y. (2013). A numerical study of nanoscale electrohydrodynamic patterning in a liquid film. *Soft Matter, 9*(12), 3412-3423.

Yarin, A. L., Koombhongse, S., & Reneker, D. H. (2001). Taylor cone and jetting from liquid droplets in electrospinning of nanofibers. *Journal of Applied Physics, 90*(9), 4836-4846.